

DEMONSTRATION OF FERROELECTRICITY IN PLD GROWN $\text{HfO}_2\text{-ZrO}_2$
NANOLAMINATES

by

Sree Sourav Das, B.S.

A thesis submitted to the Graduate Council of
Texas State University in partial fulfillment
of the requirements for the degree of
Master of Science
with a Major in Engineering
May 2021

Committee Members:

Ravi Droopad, Chair

Semih Aslan, Co-Chair

Maggie Chen

COPYRIGHT

by

Sree Sourav Das

2021

FAIR USE AND AUTHOR'S PERMISSION STATEMENT

Fair Use

This work is protected by the Copyright Laws of the United States (Public Law 94-553, section 107). Consistent with fair use as defined in the Copyright Laws, brief quotations from this material are allowed with proper acknowledgement. Use of this material for financial gain without the author's express written permission is not allowed.

Duplication Permission

As the copyright holder of this work I, Sree Sourav Das, authorize duplication of this work, in whole or in part, for educational or scholarly purposes only.

ACKNOWLEDGEMENTS

First, I would like to express my sincere gratitude towards Dr. Ravi Droopad for the opportunity to join his research group, for being my research advisor, and providing an excellent lab facility for me to conduct my research. His guidance and advice have proven invaluable in the completion of my graduate degree.

I would also like to thank the members of Dr. Droopad's research group Dr. MD. Dalim Mia, Brian Samuels, Abdul Ahad Talukdar, and Zachary Fox for their help and assistance with various measurements and analysis.

In addition, I would like to thank the rest of my thesis committee. Dr. Semih Aslan and Dr. Maggie Chen for their valuable suggestions and assistance.

The work presented in this thesis is partly funded through a donation from Intel Corp.

Lastly, I would like to thank my family for all their support over the years.

TABLE OF CONTENTS

	Page
ACKNOWLEDGEMENTS	iv
LIST OF FIGURES	vii
ABSTRACT.....	x
CHAPTER	
1. INTRODUCTION	1
2. LITERATURE REVIEW	6
2.1 Crystal Structure of HfO ₂	6
2.2 Doping Effects	8
2.3 Recent works on HfO ₂ -ZrO ₂ nanolaminates structure.....	12
2.4 Effects of deposition temperature and field cycling	15
2.5 Effects of electrodes.....	16
3. GROWTH METHOD AND CHARACTERIZATION TECHNIQUES	18
3.1 Film Deposition Technique.....	18
3.1.1 Pulsed Laser Deposition	18
3.1.2 Target Preparation.....	20
3.2 Structural & Electrical Characterization.....	21
3.2.1 X-Ray Diffraction	21
3.2.2 X-Ray Reflectivity	22
3.2.3 Filmmetrics F50 Mapper.....	23
3.2.4 Atomic Force Microscopy	25
3.2.5 Ellipsometry	26
3.2.6 Ferroelectric Measurement	28
4. GROWTH AND CHARACTERIZATION OF HfO ₂ -ZrO ₂ NANOLAMINATE SYSTEM	29
4.1 Experimental	29
4.2 Results and Discussion	33
4.2.1 Structural Analysis.....	33

4.2.2	Electrical Characterization.....	45
4.2.3	Depth Profile Analysis.....	57
5.	CONCLUSION AND FUTURE WORK.....	60
5.1	Conclusion.....	60
5.2	Future Work.....	60
	REFERENCES.....	62

LIST OF FIGURES

Figure	Page
1.1. Schematic representation of the different phases of HfO ₂ [7]	3
1.2. Qualitative model for phase transition of HfO ₂ depending on some basic factors [7]	4
2.1. Evolution of phases of HfO ₂ reproduced from ref [28]	7
2.2. Endurance vs P _r diagram from various reported results (undoped-HfO ₂ , doped-HfO ₂ , HfO ₂ -ZrO ₂ nanolaminates) [42]	10
2.3. Thickness dependent polarization variation with different dopants [7].....	11
2.4. Analysis of pure ZrO ₂ and HfO ₂ thin films (a) GIXRD scans of films with varying thicknesses and (b) P-E hysteresis curves of 12 nm ZrO ₂ and 12 nm HfO ₂	13
2.5. Analysis of ZrO ₂ /HfO ₂ and HfO ₂ /ZrO ₂ bilayer thin films (a) GIXRD scans (b) P-E hysteresis curves.....	14
2.6. Nucleation barrier height between tetragonal and monoclinic phase calculated based on classical nucleation theory.....	15
2.7. Statistics of deposition method, annealing temperature and electrodes that were used in HfO ₂ based ferroelectric film fabrication process [53].....	17
3.1. Schematic Diagram of Pulsed Laser Deposition system [59].....	19
3.2. Schematic diagram of X-ray Diffraction [60].....	22
3.3. (a) Schematic of XRR process, (b) the information(density, roughness, thickness and roughness) can be extracted from XRR are pointed out [1].....	23
3.4. Filmmetrics F-50 Mapper (Shared Research Operations, Texas State).....	24
3.5. Schematic diagram of AFM [62]	26
3.6. Schematic of spectroscopic ellipsometry [63]	27

3.7. Precision LC tester, RADIANT Technologies for ferroelectric measurement.....	28
4.1. Typical bi-layer film structure used in this study.	31
4.2. (a) XRD 2θ - ω scan of as deposited TiN, (b) AFM topological $0.5\ \mu\text{m} \times 0.5\ \mu\text{m}$ image of TiN surface	32
4.3. Electrical connection setup for ferroelectric measurement.....	33
4.4. XRD 2θ - ω scan of HfO ₂ -ZrO ₂ deposited at 750 °C and P _o =0.124 mtorr with different thicknesses.....	34
4.5. (a) Interplanar spacing of o (002) plane, (b) Normalized intensity of o (002) peak w.r.t m (-111) and (c) FWHM with varying thickness.....	35
4.6. Stacking sequence of 15 nm ZrO ₂ / 15 nm HfO ₂ where 15 nm ZrO ₂ is starting layer.....	36
4.7. XRD 2θ - ω scan of HfO ₂ starting sample (15 nm HfO ₂ /15 nm ZrO ₂) and ZrO ₂ starting layer (15 nm ZrO ₂ /15 nm HfO ₂) after deposited at 750 °C and P _o =0.124 mtorr	37
4.8. (a) Comparison of intensity of o (002) phase between ZrO ₂ starting and HfO ₂ starting samples, (b) AFM topological $0.5\ \mu\text{m} \times 0.5\ \mu\text{m}$ image of ZrO ₂ starting sample (grain size~ 43 nm).....	38
4.9. XRD 2θ - ω scans of 15 nm HfO ₂ /15 nm ZrO ₂ after deposited at 750 °C using oxygen pressures of 0.124 mtorr and 10 ⁻⁶ torr	40
4.10. XRD 2θ - ω scans of 15 nm HfO ₂ -15 nm ZrO ₂ deposited at P _o = 0.124 mtorr with different temperatures (a) after deposition and (b) after annealing at N ₂ atmosphere for 1min	41
4.11. Superlattice structure (5nm HfO ₂ /5 nm ZrO ₂) x3	43
4.12. XRD 2θ - ω scans of superlattice structure (5nm HfO ₂ /5 nm ZrO ₂) x3	43
4.13. AFM topological $0.5\ \mu\text{m} \times 0.5\ \mu\text{m}$ images of HfO ₂ -ZrO ₂ samples at different deposition conditions.	44

4.14. Ferroelectric measurement: (a) P-V hysteresis loop before field cycling, (b) P-V hysteresis loop after 10^5 field cycling, (c) Thickness dependence polarization trend, (d) Leakage test with varying thickness, (e) Endurance test, (f) Endurance up to 10^5 cycles.....	47
4.15. Ferroelectric measurement: (a) P-V hysteresis loop, (b) Leakage test for ZrO_2 starting sample and HfO_2 starting sample.....	50
4.16. Ferroelectric measurement for 15 nm HfO_2 /15 nm ZrO_2 deposited at 750 °C with different oxygen pressure.....	52
4.17. Ferroelectric measurement for 15 nm HfO_2 /15 nm ZrO_2 : (a) P-V hysteresis loop when deposited at 500 °C (b) Leakage current for 500°C and 750°C.....	53
4.18. Ferroelectric measurement for superlattice structure (5 nm HfO_2 /5 nm ZrO_2) x3	54
4.19. Summary of the effects of different growth conditions (thickness, temperature, and pressure) in terms of remnant polarization and intensity of o (002) w.r.t. m-phases	55
4.20. (a) A comparative study of remnant polarization depending upon thickness for different dopants (Undoped HfO_2 [2], HZO by ALD [3], HZO by PLD [4], Si: HfO_2 [5], Y: HfO_2 [6], Gd: HfO_2 [7]), (b) Endurance vs P_r diagram for various reported result compared with this study.....	56
4.21. Etching profile 15 nm HfO_2 /15 nm ZrO_2	58
4.22. Comparison of Zr 3d and Hf 4f peaks at different etching regions at high temperature (750°C).	59

ABSTRACT

Ferroelectricity was demonstrated for Pulsed Laser Deposition (PLD) of HfO₂-ZrO₂ bilayer thin films grown on TiN bottom electrodes on SiO₂/Si as a function of deposition conditions and individual HfO₂-ZrO₂ layer thicknesses. Thicknesses of individual layers in HfO₂-ZrO₂ bilayer system were varied from 5 nm to 15 nm, deposition temperature was varied from room temperature to 750°C and partial oxygen pressure was varied from 10⁻⁶ torr to 0.124 mtorr. The films deposited at higher temperature, higher pressure and have higher thicknesses showed better ferroelectric response with 12 μC/cm² remnant polarization and 10⁻⁷ A leakage current (at 8 V) with endurance greater than 10¹¹ cycles indicative of an orthorhombic crystal phase. On the other hand, films deposited at lower temperatures and pressures did not exhibit ferroelectric behavior. These films were determined to have a monoclinic structure, lower grain size and higher leakage current. The effects of ZrO₂ layer were also demonstrated by changing the sequence in the structure and it was found that ZrO₂ as the top layer provided better mechanical confinement for stabilizing the orthorhombic phase. Finally, the effect of the interfacial layer between HfO₂-ZrO₂ nanolaminates was investigated by depth profile analysis and a bilayer structure was proposed with proper process conditions and layer thicknesses that could potentially exhibit higher remnant polarization and strong endurance against fatigue for memory applications.

1. INTRODUCTION

The demand for memory devices has reached an unprecedented peak due to the scale and complexity of data storage with emerging technologies. Better data storage with minimal space can be achieved by miniaturization. Since the discovery of ferroelectricity in HfO₂-ZrO₂ nanolaminates stacking structure, they have been considered as the best candidate for future ferroelectric Random-Access Memories. Several ferroelectric materials including triglycine sulfate [8] and similar compounds, potassium di-hydrogen phosphate[9], Rochelle salt[10], etc. have been studied over the past several decades. Among them, perovskite and related structures such as BaTiO₃, PbTiO₃, SrBi₂Ta₂O₉, Bi₄Ti₃O, PZT etc. [11]–[17] have attracted a great of attraction because of their chemical and thermal stability. Moreover, they also show large remnant polarization, high dielectric constant and better electro-mechanical response. Despite having excellent characteristics, perovskite materials show deterioration in their properties with downsizing and are challenging to integrate in devices because of their complicated structure. These setbacks increase fabrication cost of perovskite based-ferroelectric memories over charged-based technology. Furthermore, these materials are not compatible with silicon technology because, during high temperature annealing under H₂ environment, H⁺ can incorporate into the perovskite structure resulting in degraded performance. So, a new type of ferroelectric has been in constant demand which can overcome scaling problems along with better compatibility with Si. Recently, ferroelectricity has been found on hafnium oxide-based materials which demonstrate high remnant polarization without deterioration with downsizing on the order of 10 nm; even in 5 nm due to its high bandgap (5-5.9eV) compared to PZT and other related perovskite

materials with bandgaps of 3-4 eV [18]. In addition to scalability, they can be used as gate dielectric layers instead of silicon dioxide because of the high compatibility with Si and its high dielectric constant. For example, ferroelectric FETs with 28 nm of high-k gate oxide of Si-doped HfO₂ have already been fabricated [19]. Highly integrated HfO₂-based ferroelectric memories are also feasible because of its chemical structure, outstanding polarization switching and endurance performance at the nano-scale level.

At room temperature, HfO₂-based materials are stable with a monoclinic phase (m-phase) which has lower symmetry and transforms into higher symmetry tetragonal phase at an elevated temperature of 1720°C and this tetragonal phase (t-phase) transforms into cubic phase (c-phase) with a further increase in temperature to 2700°C. However, these phases are centrosymmetric and not responsible for the ferroelectricity in HfO₂. Previous studies suggest that ferroelectricity in HfO₂ originates from the non-centrosymmetric orthorhombic phase (o-phase) with space group Pca₂₁, as shown in figure 1.1 which was first proposed in Mg-doped ZrO₂ with neutron diffraction and also confirmed by Sang et al. using scanning transmission electron microscopy (STEM)[20]–[22].

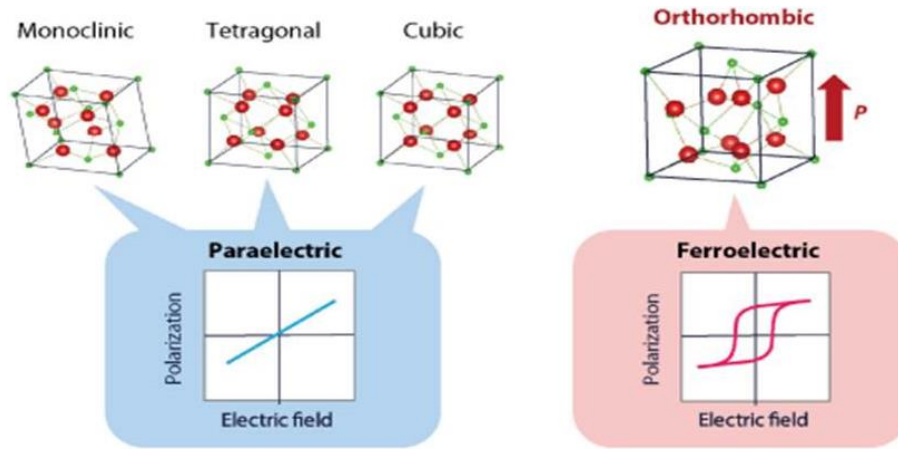


Figure 1.1: Schematic representation of different phases of HfO_2 . Red denotes Oxygen atoms and green denotes Hafnium atoms in the structure [7].

This o-phase is not stable at room temperature, but it is found as an intermediate phase between monoclinic and tetragonal phase during cooling. Sometimes, it also coexists with the monoclinic phase. To stabilize this ferroelectric phase at room temperature, HfO_2 can be prepared by chemical doping using Y, Zr, Si, Al, La, Gd and other metal elements via various deposition techniques including atomic layer deposition (ALD), physical vapor deposition (PVD), chemical vapor deposition (CVD), sputtering, chemical solution deposition (CSD), and pulse laser deposition (PLD). In fact, pure HfO_2 and ZrO_2 can also show ferroelectricity when certain conditions are satisfied [2], [23], [24]. With the increasing doping concentration in HfO_2 , the non-ferroelectric m-phase transforms to t-phase if the dopant atoms are smaller than Hf atom like Si, Al or to c-phase if the dopant atoms are bigger than Hf atom like Y, Zr, Gd and Sr [25]. Furthermore, the relative amount of orthorhombic phase over monoclinic phase depends on some other factors such as annealing conditions, bottom electrode, oxygen vacancies, capping layer, and film thickness. Recently, a model has been proposed to describe the crystallization of the film depending on the basic factors illustrated in figure 1.2 [26]. The

monoclinic phase dominates at lower doping concentration and higher film thickness, the opposite leads to t-/c-phase with the ferroelectric orthorhombic phase exists at boundary of the paraelectric phases.

Researchers have recently started to investigate a new design comprising of HfO₂-ZrO₂ bilayer/superlattice where ZrO₂ as the top layer creates mechanical stress over HfO₂ to suppress tetragonal to monoclinic transformation, resulting in a stable orthorhombic phase with higher remnant polarization as well as strong endurance up to 10¹⁰ cycles. However, this system is not well-studied system and ALD is the only deposition technique that has been used so far to study this HfO₂-ZrO₂ nanolaminates system. So, to further validate the behavior of ferroelectricity in this nanolaminates system and study employing different growth techniques can be carried out where the growth conditions (temperature, oxygen pressure, thickness, etc.) can be varied to confirm and maximize the ferroelectric response in the structure.

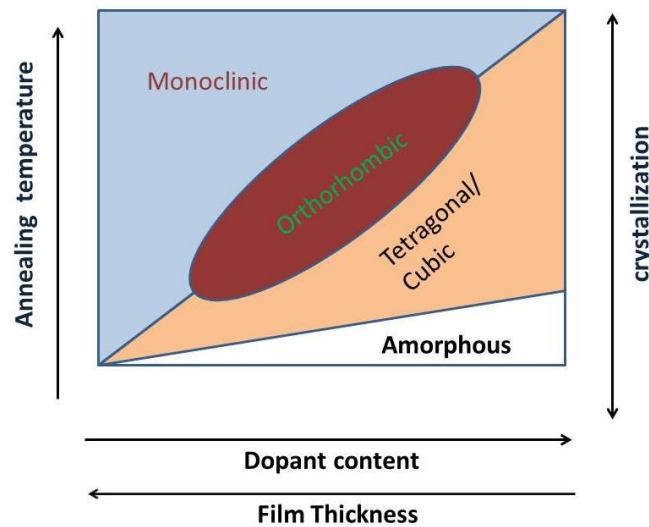


Figure 1.2: Qualitative model for phase transition of HfO₂ depending on some basic factors [7].

The objective of this thesis is to study ferroelectricity in PLD grown $\text{HfO}_2\text{-ZrO}_2$ bilayer system by optimizing the growth conditions (substrate temperature, partial oxygen pressure, pulse rate, etc.). The structure and ferroelectric properties of PLD grown $\text{HfO}_2\text{-ZrO}_2$ nanolaminates, including remnant polarization, endurance, and fatigue test will be investigated, and compared with ALD grown films. The outcome of this study will increase the understanding and suggest possible routes to optimize this material system for memory applications.

2. LITERATURE REVIEW

2.1 Crystal Structure of HfO₂

Since the discovery of the ferroelectric o-phase in HfO₂, researchers have been trying to find the answer to one question: how does this o-phase stabilize in HfO₂ among the competitive phases like t-phase, c-phase, and m-phase, and how to control this o-phase to get better ferroelectric response? It is believed that the o-phase and t-phase has similar lattice structure. The lattice parameters of HfO₂ in distinct phases from previous experimental results are shown in table 2.1 [27]. For example, the lattice parameters of the o-phase HfO₂ are $a=5.22\text{\AA}$, $b=5.02\text{\AA}$, $c=5.04\text{\AA}$ and $a=5.06\text{\AA}$, $b=5.06\text{\AA}$, $c=5.20\text{\AA}$ for the t-phase HfO₂. Therefore, the a-axis of the o-phase can be obtained by stretching the c-axis of the t-phase while the b- and c-axis of the o-phase can be obtained by compressing the a- and b-axis of the t-phase. In this conception, tensile and compressive stress are required to apply along a or b axis and c-axis, respectively, for the transition from t-phase to o-phase. Researchers investigated and concluded some driving factors (thickness, temperature, doping, etc.) that can play significant roles to create this anisotropic stress on the film to stabilize the ferroelectric phase in the film as depicted in figure 2.1. By controlling the driving factors, it is possible to stabilize the orthorhombic phase at room temperature.

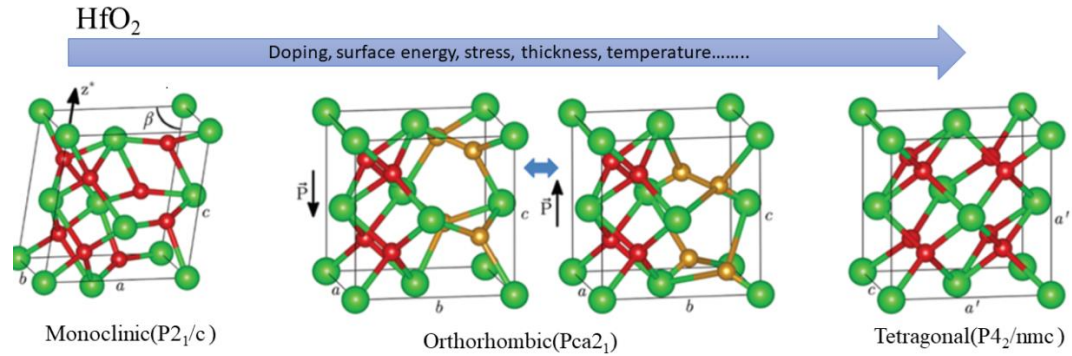


Figure 2.1: Evolution of phases of HfO₂ reproduced from ref [28].

Among the driving factors that determines stability of ferroelectricity in pure HfO₂ or doped HfO₂, film thickness and annealing temperature are the most two dominant ones. This is because film thickness and annealing temperature controls the grain size of the film. With increasing film thickness and annealing/deposition temperature, the grain size increases and so, bulk energy dominates over the surface energy which increases paraelectric m-phase in the film over the orthorhombic phase. Recent studies suggest that orthorhombic or tetragonal phase is more stable in HfO₂ when the grain size is less than 4 nm [29]. Grain sizes for the o-phase in HfO₂ could be increased to 16 nm by Zr-doping [27] or to 27 nm by Si-doping [30]. Alternatively, Al₂O₃ was also used in a HZO/Al₂O₃/HZO multilayer structure where the thickness of the individual HZO layer was 10 nm and Al₂O₃ controls the grain of HZO films as well as stabilize the o-phase in the film [31]. Along with grain size, oxygen vacancies also play an important role in stabilizing the orthorhombic phase. Orthorhombic or tetragonal phase could be stabilized over the m-phase in the presence of oxygen vacancies [32]. Larger fraction of oxygen vacancies was observed in Gd-doped HfO₂ grown on TaN than TiN electrode which increased the polarization in the film, although it results in a decrease of the endurance in the film [7]. There are some other factors which are also

responsible for the ferroelectricity in the film i.e. top/bottom capping layer electrode, thermal expansion mismatch [22], etc.

Table 2.1: Summary of reported results on lattice constant of separate phases of HfO₂ [27]

Structure	a(Å)	b(Å)	c(Å)
m-HfO ₂	5.12	5.17	5.29 [33]
	5.07	5.14	5.29 [5]
	5.11	5.16	5.28 [34]
	5.09	5.16	5.26 [35]
t-HfO ₂	5.06	-	5.20 [33]
	5.06	-	5.20 [5]
	5.03	-	5.12 [34]
	4.90	-	4.95 [35]
f-HfO ₂	5.22	5.02	5.04 [33]
	5.07	4.88	4.89 [5]
	5.30	5.10	5.11 [34]
	5.29	5.01	5.08[35]

2.2 Doping Effects

Over the past few years, different types of doping were used to stabilize the ferroelectricity in HfO₂. Among them, the most intensively studied system was the HfO₂-ZrO₂ alloy/solid solution as these binaries have similar ionic size and chemical valence.

Moreover, the main reason for this increasing interest in HZO is more compatible with a conventional CMOS flow than other ferroelectric materials. Recent studies show ferroelectricity over a wide composition range and the remnant polarization in $\text{Hf}_x\text{Zr}_{1-x}\text{O}_2$ peaked at $x=0.5$. Crystallization temperatures for $\text{Hf}_{0.5}\text{Zr}_{0.5}\text{O}_2$ is also significantly lower ($T \approx 400^\circ\text{C}$) compared to pure HfO_2 and pure ZrO_2 . Combining these factors, it is believed that $\text{Hf}_{0.5}\text{Zr}_{0.5}\text{O}_2$ in non-volatile ferroelectric memories is an extremely promising candidate. Additionally, $\text{Hf}_{0.5}\text{Zr}_{0.5}\text{O}_2$ shows strong correlation between polarization and film thickness, especially, among the thin films ranging from 5.5 nm to 25 nm [36]. Temperature dependent ferroelectric transition was also observed in Zr-rich HZO film where higher temperature increased the leakage current and anti-ferroelectricity in the film. Moreover, a significant amount of m-phase and t-phase is also present in the Zr-rich films which degrades the FE-performance. ZrO_2 or Zr-rich HZO film also shows higher coercive field [37] which increases the driving electric field to exploit the full P_r values. This driving field is close to the breakdown field of the material. So repeated cycling can induce electrical breakdown before the fatigue test is completed, therefore, such composition shows low cycling endurance ($\sim 10^8$ cycles at 2.5MV/cm). Figure 2.2 and figure 2.3 summarize the endurance results and thickness dependency of polarization reported to date by different researchers for undoped HfO_2 [2], [31] Si-doped HfO_2 [7], [19], [25], Al-doped HfO_2 [38], Si and Al-co-doped HfO_2 [39], $\text{Hf}_x\text{Zr}_{1-x}\text{O}_2$ [18], [40], [41], and Gd-doped HfO_2 [7] as well as HfO_2 - ZrO_2 nanolaminates system [42]. Among different dopants, Gd-doped HfO_2 showed the highest remnant polarization ($2P_r$) of $35\mu\text{C}/\text{cm}^2$ but it could endure up to 5×10^5 cycles which is not enough for memory applications [7]. Like Gd-doped HfO_2 , although undoped HfO_2 could provide high

remnant polarization ($10\mu\text{C}/\text{cm}^2$ at 6nm) in lower thicknesses, endurance was only 10^6 cycles for undoped HfO_2 [2]. On the other hand, Zr-doped HfO_2 endured up to 4×10^{10} cycles with $10\mu\text{C}/\text{cm}^2$ remnant polarization by introducing STO (100) template and it was also possible to maximize polarization up to $20\mu\text{C}/\text{cm}^2$ by reducing the thickness of HZO film as shown in figure 2.3. However, STO is a perovskite material like PZT which also increases the complexity in the integration process.

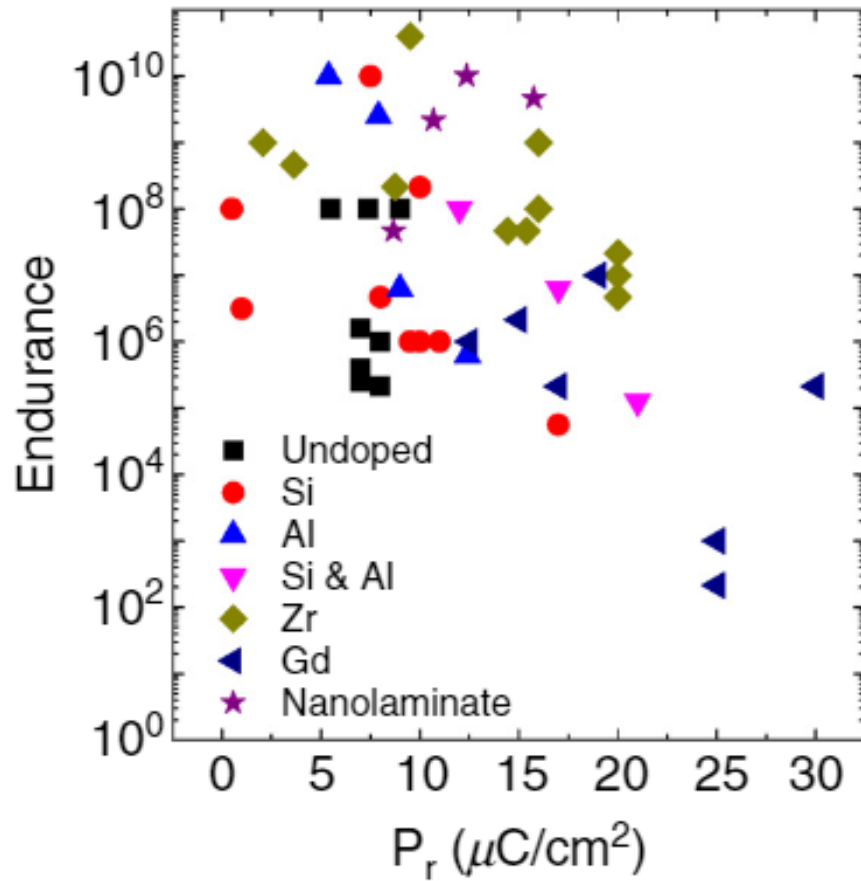


Figure 2.2: Endurance vs P_r diagram from various reported results (undoped- HfO_2 , doped- HfO_2 , HfO_2 - ZrO_2 nanolaminates) [42].

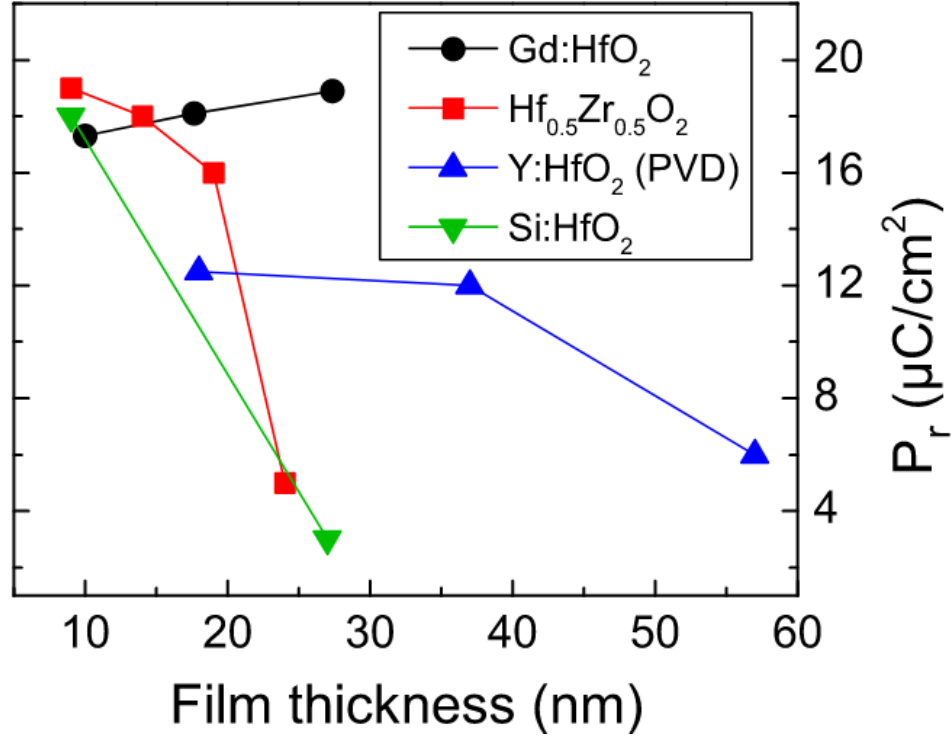


Figure 2.3: Thickness dependent polarization variation with different dopants [7].

Polarization in Gd-doped HfO₂ increases with thicknesses which is quite opposite with compared to other dopants. The maximum and minimum polarization was obtained for thicknesses of 27 nm and 10 nm, respectively [7]. Other than Gd-doped HfO₂, Zr-doped, Y-doped, and Si-doped showed a downward trend with increasing thicknesses because of increasing m-phase or c-phase with thickness. All the dopants have induced around 10-35 μC/cm² remnant polarization except La-doped HZO (45 μC/cm²), but still, it is smaller than theoretical values (50-60 μC/cm²). These films exhibit mixed phases of o-phase and m-phase or t-phase rather than the pure ferroelectric o-phase. Besides, in case of doped HfO₂, precision composition control was needed to get higher remnant polarization as well as strong endurance which increases the difficulty in the fabrication process. Considering the limitation of undoped and doped HfO₂, researchers recently

developed a new structure, called HfO₂-ZrO₂ nanolaminates, that showed moderate amount of remnant polarization with endurance up to 10¹⁰ cycles [42]. The nanolaminates samples showed similar level of endurance as Zr-doped films with higher polarization. Additionally, the undoped HfO₂-ZrO₂ bilayer thin film is simpler in design and the fabrication process becomes easier than doped HfO₂ or HfO₂-ZrO₂ solid solution in which precise composition control omits the design flexibility. Therefore, the HfO₂-ZrO₂ nanolaminates system is a promising candidate for memory applications with their strong endurance against fatigue.

2.3 Recent works on HfO₂-ZrO₂ nanolaminates structure

Ferroelectricity in nanolaminates of HfO₂-ZrO₂ was first introduced by ALD at 150°C on Pt/Ti/SiO₂/Si substrate and annealed afterwards in N₂ atmosphere at 600°C for 20s for crystallization. Thickness of the individual layers was varied from 1.5 nm to 12 nm [43]. To understand the behavior of HfO₂-ZrO₂ bilayer system, a single layer of HfO₂ and ZrO₂ was studied first to optimize the design. Size-dependent phase transition was confirmed by GIXRD in pure HfO₂ and ZrO₂. A low-symmetry paraelectric m-phase in pure HfO₂ increases with increasing film thickness as shown in figure 2.4 (a). The polarization P-E hysteresis curve for 6 nm HfO₂ and 12 nm HfO₂ also shows a linear dielectric behavior with no hysteresis. On the other hand, a 12 nm thick ZrO₂ layer shows a propeller-shaped hysteresis curve with non-zero remnant polarization which indicates the anti-ferroelectricity like behavior as shown in figure 2.4(b). Recent studies suggest this phenomenon can be attributed to the electric field induced tetragonal to non-ferroelectric orthorhombic (III) phase transition [44]. Also, there might be a strong depolarization effect at low electric field due to the non-ferroelectric phase.

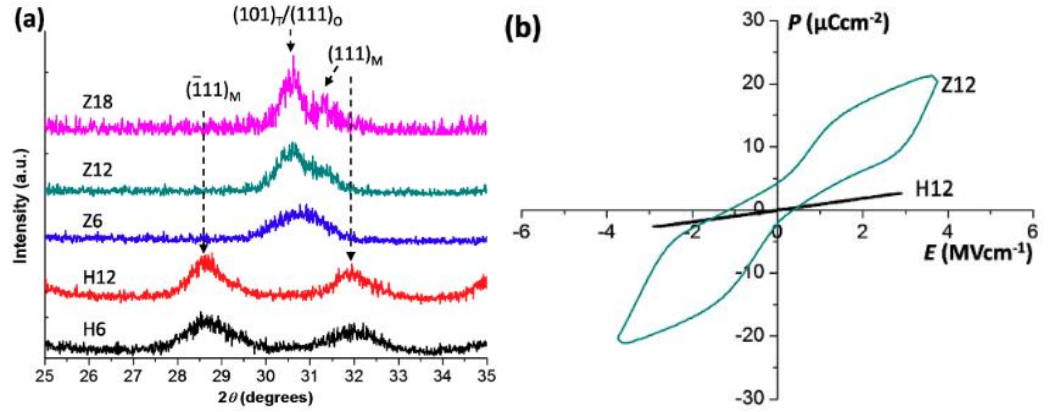


Figure 2.4: Analysis of pure ZrO_2 and HfO_2 thin films (a) GIXRD scans of films with varying thicknesses and (b) P-E hysteresis curves of 12 nm ZrO_2 and 12 nm HfO_2

In the case of a double layer structure, ZrO_2 (Z6H6: 6 nm ZrO_2 / 6 nm HfO_2) as a top layer provides thermal stress and better mechanical confinements than in H6Z6 (ZrO_2 as bottom layer). When ZrO_2 is deposited as the top layer, because of higher degree of crystallization than HfO_2 , it crystallizes before the underlying HfO_2 layer during annealing and HfO_2 experiences a large thermal stress resulting in a transformation to the higher-pressure o-phase. Thickness of the top ZrO_2 was also varied from 1.5 nm to 6 nm. With the increasing thickness of ZrO_2 , the crystal size also increases, leading to increased confinement of the HfO_2 layer and promoting a larger fraction of the o-phase in the HfO_2 layer as shown in figure 2.5. On the other hand, ZrO_2 as starting layer create in-plane tensile stress on the top HfO_2 layer because of having larger lattice parameters than HfO_2 . The stress was calculated from Gaussian fitting of the XRD peaks of HfO_2 - ZrO_2 nanolaminates and plotted in figure 2.6. The energy barrier height (E_a) for the $t \rightarrow m$ -phase transition decreases with increasing of stress. Therefore, bulk-free energy difference would increase and make m-phase more stable. Again, increasing bulk-free

energy difference decreases the critical radius of m-phase nucleation. Thus, nucleation rate of m-phase in the t-phase matrix would increase with tensile stress.

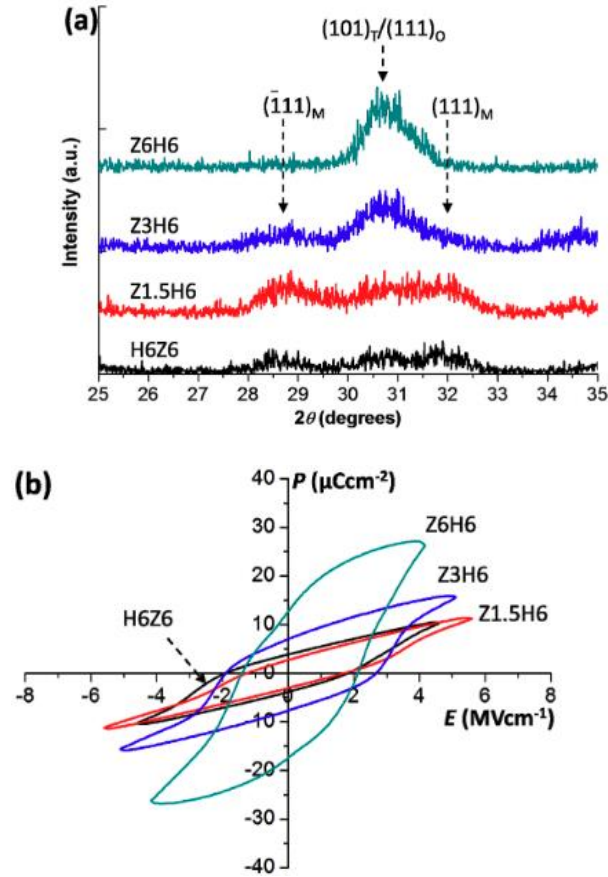


Figure 2.5: Analysis of $\text{ZrO}_2\text{-HfO}_2$ and $\text{HfO}_2\text{-ZrO}_2$ bilayer thin films (a) GIXRD scans (b) P-E hysteresis curves.

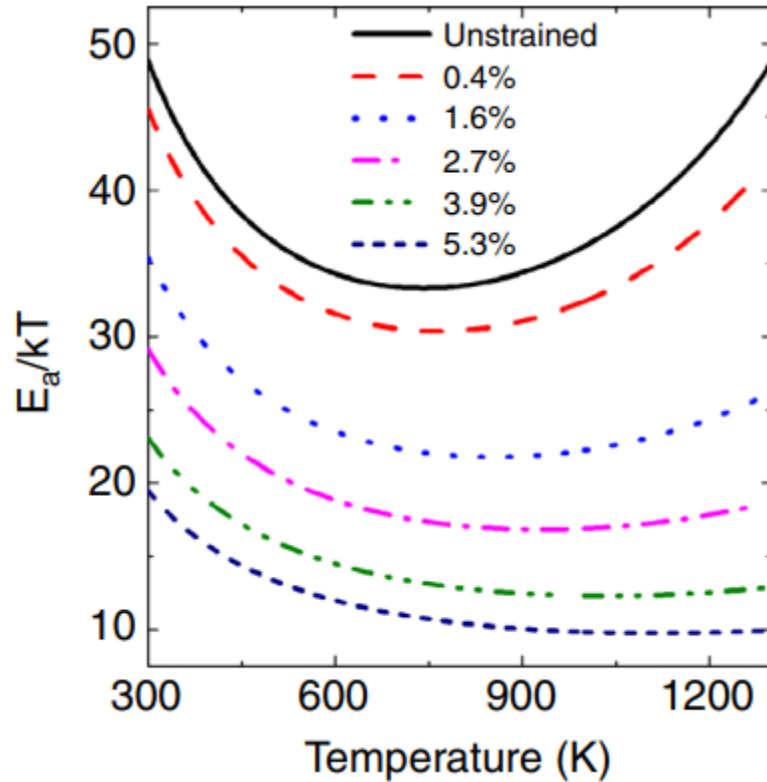


Figure 2.6: Nucleation barrier height between tetragonal and monoclinic phase calculated based on classical nucleation theory.

2.4 Effects of deposition temperature and field cycling

Deposition temperature and electric field cycling are also needed to be considered for the phase stabilization and transformation in the nanolaminates. Samples that are deposited by ALD at a low temperature (i.e., 260°C [45]) showed antiferroelectric-like response for the as-deposited devices whereas nanolaminates deposited at higher deposition temperature (i.e. 285°C [45]) crystallized into the orthorhombic phase and exhibited a ferroelectric response. It was concluded that nucleation of crystallites increased significantly with increasing deposition temperature for which o-phase favored in higher temperature deposited films. Field induced phase transition from antiferroelectric to ferroelectric was also observed in the films that are deposited at lower

temperature. This trend is attributed to oxygen vacancies distribution. The o-phase is sensitive to oxygen vacancy concentration and field cycling was proposed to redistribute the vacancies from electrode-film interface to bulk leading to crystallographic transition of the ferroelectric phase [45].

2.5 Effects of electrodes

Electrodes also play a critical role for the stabilization of ferroelectricity by applying mechanical stress because it can affect the grain size and the orientation of ferroelectric films. Several types of electrodes have been investigated including TiN, Ru [46], [47], Ir [39], [48], TaN [7], LSMO [18], Pt [49], and so forth for the mechanical confinement required for the formation of the unstable o-phase. But no improvement compared to TiN has not been reported so far, as shown in figure 2.7. Ir/IrO_x as electrodes has been used successfully to solve the fatigue issue of PZT [50], but in case of Si-doped HfO₂ thin films, this electrode provide 13-14 $\mu\text{C}/\text{cm}^2$ less P_r compared to TiN capped capacitor because coefficient of thermal mismatch and the potential scavenging effect of TiN [39]. On the other hand, Gd-doped HfO₂ thin films with a TaN capped capacitor provide higher P_r than TiN because of the large concentration of the oxygen vacancies, but these vacancies can increase the leakage current and built-in field which suppresses the nucleation of domains with the opposite polarity [51]. In fact, TiN crystallizes at low temperature (preferably <500°C [52]) where high annealing temperature drives an undesirable phase transition from o-phase to m-phase [52] and it is less inclined to form oxynitrides [7]. Moreover, TiN acts a barrier layer against H-diffusion during forming gas annealing [62]. Thus, TiN can be considered as the best candidate for both the bottom and top electrodes. Statistics of different deposition

methods, annealing temperature, and electrodes have been used so far for HfO₂-based ferroelectrics is shown in figure 2.7 [53]. Among different deposition methods, ALD is the most popular technique for HfO₂ based film and lower deposition temperature was used. In comparison to ALD, PLD technique remains less-studied for HfO₂-based materials, specifically, in the field of nanolaminates. Moreover, PLD has better flexibility in changing deposition pressure and temperature in wide range compared to ALD. Thus, it is possible to optimize the bilayer structure for memory applications with increased ferroelectricity by controlling the deposition pressure, temperature, and growth rate.

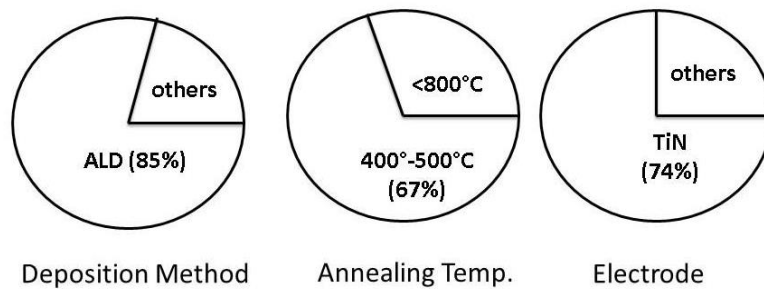


Figure 2.7: Statistics of deposition method, annealing temperature and electrodes that were used in HfO₂ based ferroelectric film fabrication process [53].

3. GROWTH METHODS AND CHARACTERIZATION TECHNIQUES

In this chapter, the pulsed laser deposition (PLD) process is described as the main deposition technique used in this study for the growth of HfO₂ and ZrO₂ thin films. The crystal structure and phases of the thin films were investigated by X-ray diffraction measurements on a Rigaku SmartLab system with Cu anode. Four-crystal monochromator Ge (220) was used to eliminate the vertical divergence and K α ₂ line leaving only K α ₁ component. The thicknesses of the films were measured by using the X-ray reflectivity on a Rigaku SmartLab system, variable angle spectroscopic ellipsometry using J.A. Wollam, M-2000 ellipsometer and a Filmmetrics F-50 Mapper. Surface morphology of bottom electrode was measured by atomic force microscopy. Finally, ferroelectricity was analyzed using a ferroelectric tester from Radiant Technologies.

3.1 Film Deposition Technique

3.1.1 Pulsed Laser Deposition

Pulsed laser deposition is a technique which is used to deposit thin films by means of a powerful focused pulsed laser striking on the surface of target to melt, evaporate and ionize the material and transferring the desired composition on the substrate [54]–[56]. PLD became a well-known technique in the thin film deposition technology since the discovery of the first superconductive YBCO film at Bell Communication Research [57], [58]. A schematic diagram of a PLD system is shown in Figure 3.1 [59].

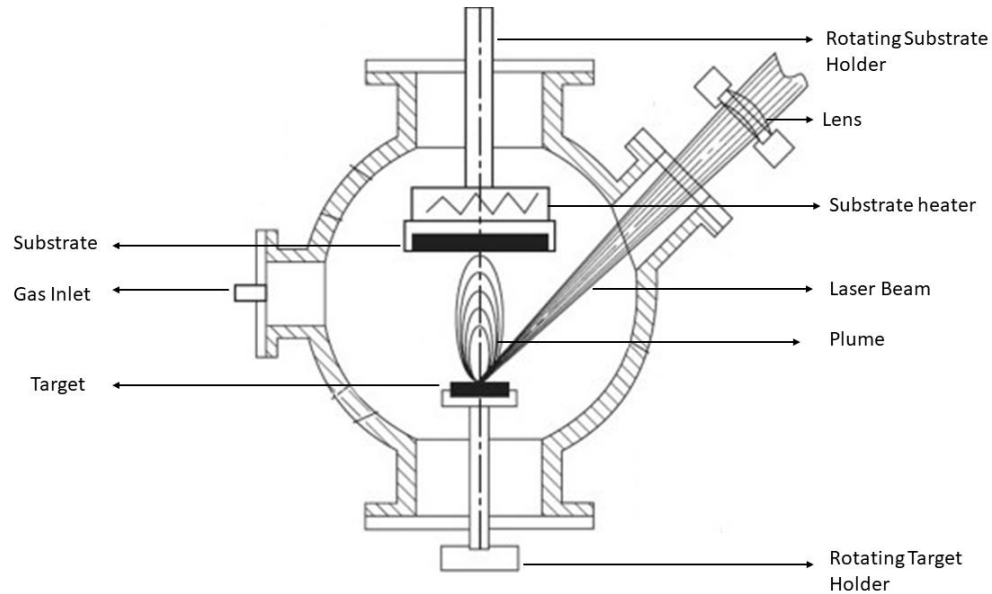


Figure 3.1: Schematic Diagram of Pulsed Laser Deposition system [59].

The main components of PLD system are the substrate and the target holders. The target is rotated by a motor to prevent irregular target erosion due to laser scanning/rastering and substrate is rotated to obtain uniform deposition of the material over the substrate. In the system used for this study, a load lock is used to load both the substrate and target into the deposition without the need to expose the chamber to atmosphere. The chamber pressure is controlled by turbo molecular pump which can achieve chamber pressures as low as 10^{-9} torr. However, different types of gas can be introduced into the chamber during deposition and chamber pressure can be maintained by both controlling the gas flow and speed of turbo pump. The laser beam strikes the surface of the target at a 45° angle and can be focused using a quartz lens.

In principle, PLD is one kind of physical vapor deposition technique where a pulsed UV radiation from a high-powered excimer source hits the target to ablate the material. Due to the high energy of laser, atoms from the target evaporate with high

kinetic energy (5-100eV) and adhere to the surface of the substrate. PLD has several advantages in comparison to other deposition techniques. Firstly, the deposited materials on substrate can have the same stoichiometry of target. Secondly, PLD gives flexibility over a wide range of pressure during deposition that could range from ultra-high vacuum (10^{-9} torr) to low vacuum (10^{-2} torr) and so, it is possible to optimize the growth conditions i.e., substrate temperature, chamber pressure, pulse rate, etc. to obtain the desired film quality. Thirdly, it is possible to grow complex multilayer thin films easily with the help of a programmable rotation system for changing the targets.

In this study, a PLD system with COMPex Pro KrF excimer laser of 248 nm wavelength is used for the deposition of the HfO₂/ZrO₂ multilayer structures.

3.1.2 Target Preparation

For PLD, a hard and dense target is required as a source on which laser pulse will strike and ablate the material. To prepare the targets for PLD highly pure oxide powders were weighed and mixed with appropriate weight/atomic ratio. An ultrasonic ball miller was used for 30-40 min to mix the powders homogeneously. Later, the mixed powder was placed into a mold and pressed using a hydraulic press for 20 hours at a temperature of 450 °C and a pressure of 19000 lb/in² to create 1-inch ceramic disk. The disk is then sintered in a tube furnace at 1000 °C in argon gas for 20 hours resulting in a dense target that can be used for deposition by PLD.

3.2 Structural & Electrical Characterization

3.2.1 X-Ray Diffraction

X-ray diffraction (XRD) is a non-destructive analytical technique that can be used to determine the structural properties of various materials including powder, liquids, and crystalline films. This technique can reveal the information about crystal structure, crystal quality, orientation, stress, etc. X-rays are electromagnetic waves with wavelength only of the order of 0.1 nm. X-rays incident on a crystalline solid will be diffracted by crystalline plane as demonstrated in figure 3.2. Diffracted beams with the same wavelength can either reinforce or cancel each other. When they have path difference of $n\lambda$, called ‘in-phase’, constructive interference occurs which is described by Bragg’s Law of Diffraction:

$$n\lambda = 2d\sin\theta \quad 3.1$$

In this equation, n is the integer which represents the order of diffraction peaks, λ defines the wavelength of the x-rays, θ is the incident angle of the x-rays relative to the sample normal and d is the interplanar spacing.

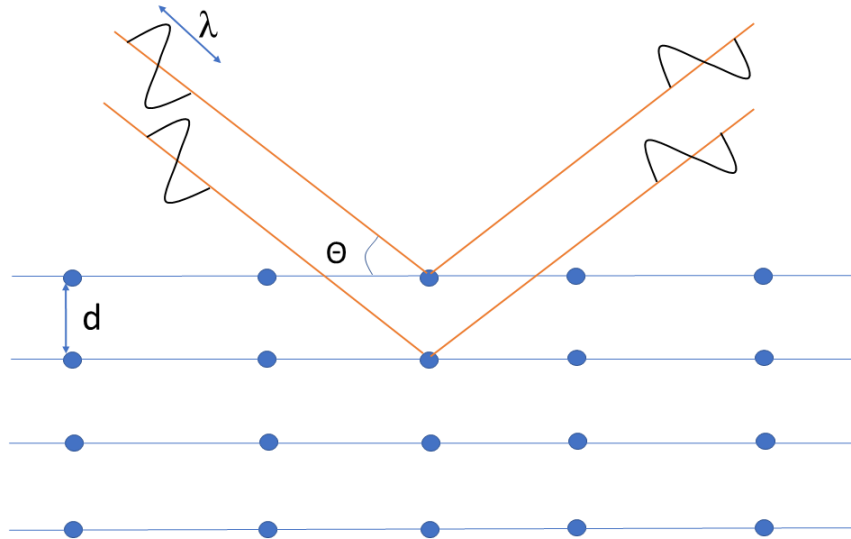


Figure 3.2: Schematic diagram of X-ray Diffraction [60]

The diffracted rays are detected by a detector where the intensity was measured and plotted with respect to the incident angles θ . The resulting spectrum is then compared to a crystallographic database to obtain the structural properties of the materials.

In this experiment, a Rigaku Smart-Lab X-ray diffractometer with operating voltage of 40 kV and current of 44 mA for Cu-K α source having wavelength of $\lambda = 1.540562 \text{ \AA}$ was used for crystal structure identification.

3.2.2 X-Ray Reflectivity

Unlike XRD, X-ray reflectivity (XRR) is used to measure the thin film parameters including thickness, density and surface or interface roughness. It can be used to study opaque film as well as multi-layer film. In case of XRR, X-rays is incident on the surface at a grazing angle that is smaller than the critical angle and undergo total internal reflection. All the X-rays are reflected from the surface when they are incident at or lower than critical angle (θ_c) as shown in Figure 3.3. With the increment of incident angle, X-

rays started to penetrate the material through refraction. When X-rays reflected from the surface, these are collected by a detector and create an interference and oscillation pattern in the spectrum. Thicker or denser film shows more oscillation than thinner or less dense film and rougher film shows higher decay in the reflected spectrum than smoother film [61]. By applying by a mathematical model to the spectrum, it is possible to obtain the thickness, density, and roughness of the film.

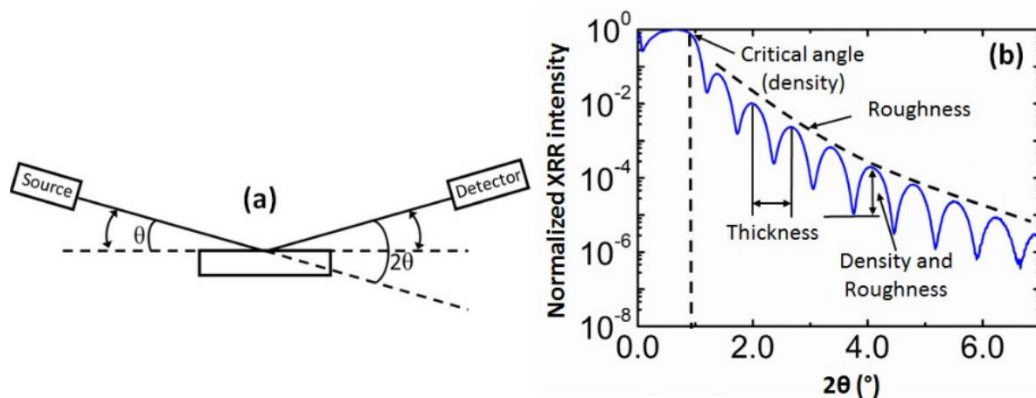


Figure 3.3: (a) Schematic of XRR process, (b) the information (density, roughness, thickness and roughness) can be extracted from XRR are pointed out [1].

3.2.3 *Filmetrics F50 Mapper*

The Filmetrics F50, shown in figure 3.4, is an automated thin-film thickness mapping system equipped with a motorized θ -stage that moves automatically to selected measurement points and provides thickness measurements as fast as two points per second. The system is capable of mapping wafers using predefined polar, rectangular, or linear map patterns with center or edge exclusion. The Filmetrics F50 is used to measure thickness of dielectrics, semiconductors, and thin (~ 10 nm) metal films. The measured films must be smooth and between 10 nm and 70 microns thick. Optical

constants, n , and k can also be measured on a variety of dielectric films. Commonly measured films include oxides, nitrides, and photoresists. Films that cannot be measured include very rough films and thick metal films.



Figure 3.4: Filmetrics F-50 Mapper (Shared Research Operations, Texas State)

3.2.4 Atomic Force Microscopy

The Atomic Force Microscopy (AFM) was developed to overcome the drawback of STM (Scanning Tunneling Microscopy). The AFM has the advantage of imaging almost any type of surface, including polymers, ceramics, composites, glass, and biological samples.

An AFM uses a cantilever with a very sharp tip to scan over a sample surface. As the tip approaches the surface the close-range, attractive force between the surface and the tip causes the cantilever to deflect towards the surface. However, as the cantilever is brought even closer to the surface, such that the tip contacts it, increasingly repulsive force takes over and causes the cantilever to deflect away from the surface. A laser beam is used to detect these cantilever deflections towards or away from the surface. By reflecting an incident beam off the flat top of the cantilever, any cantilever deflection will cause slight changes in the direction of the reflected beam [62]. A position-sensitive photo diode (PSPD) can be used to track these changes as shown in figure 3.5. Thus, if an AFM tip passes over a raised surface feature, the resulting cantilever deflection (and the subsequent change in direction of reflected beam) is recorded by the PSPD. An AFM images the topography of a sample surface by scanning the cantilever over a region of interest. The raised and lowered features on the sample surface influence the deflection of the cantilever, which is monitored by the PSPD. By using a feedback loop to control the height of the tip above the surface—thus maintaining constant laser position—the AFM can generate an accurate topographic map of the surface features.

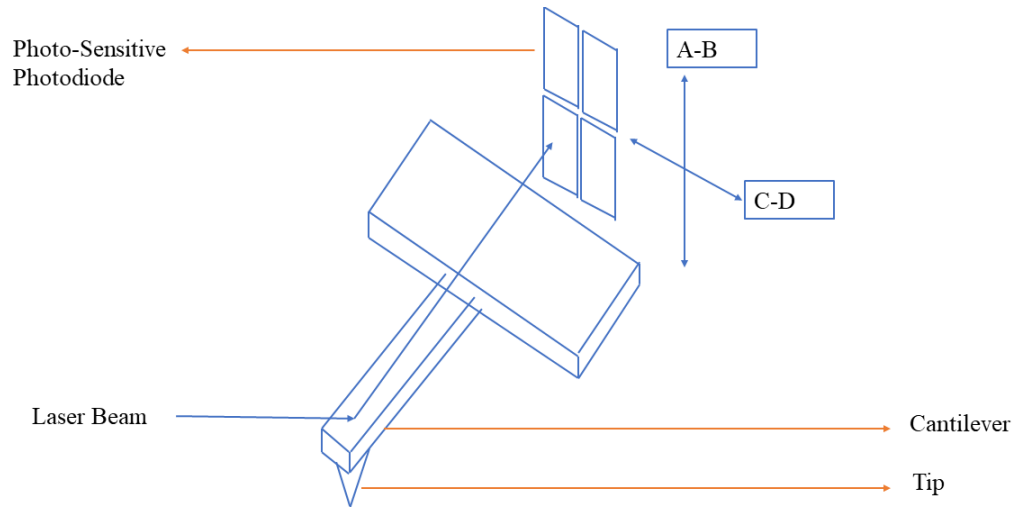


Figure 3.5: Schematic diagram of AFM [62].

3.2.5 Ellipsometry

Ellipsometry is a non-destructive spectroscopic technique that is used to directly determine the thickness, roughness, and optical constant of single/multilayer films. Ellipsometry measures a change in the polarization state as light reflects or transmits from a material structure. The polarization change is represented as an amplitude ratio, Ψ , and the phase difference, Δ . The measured response depends on optical properties and thickness of individual materials. However, it is also applied to characterize composition, crystallinity, roughness, doping concentration, and other material properties associated with a change in optical response.

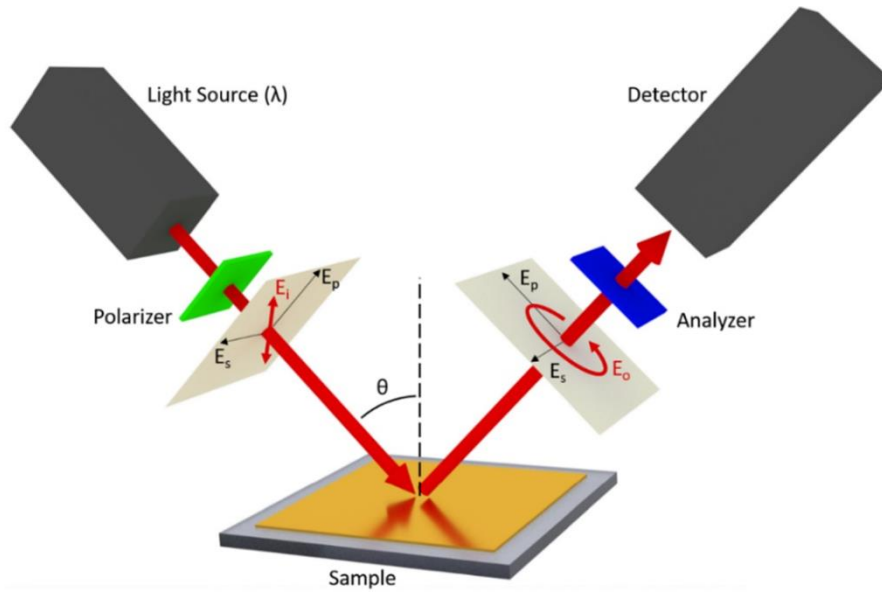


Figure 3.6: Schematic of spectroscopic ellipsometry [63]

A linearly polarized light is incident on the sample surface and reflected or transmitted from the sample with changes in polarization that can be measured as shown in Figure 3.6. The change in the polarization is ellipsometry measurement is commonly written as,

$$\rho = \tan(\Psi) e^{i\Delta} \quad 3.2$$

Where, $\tan(\Psi)$ is the amplitude ratio of the p- and s-polarized light and Δ is the phase difference. A light source produced unpolarized light and it is sent through a polarizer where the light becomes linearly polarized. The linearly polarized light becomes elliptically polarized light after reflecting from the surface and travels through the analyzer. Then, the detector converts the light into electronic signal to measure the reflected polarization.

3.2.6 *Ferroelectric Measurement*

P-E hysteresis loop provides the confirmation of ferroelectricity in the film. Remnant polarization, coercive field, endurance, and leakage current are the main factors to define the quality of a ferroelectric material. The RADIANT ferroelectric analyzer, as shown in figure 3.7, was employed for ferroelectricity measurements during this study. A 16 V peak-peak triangular wave with 1 ms period was applied to sample for the measurement of remnant polarization and coercive field. For endurance, 10^{12} cycles of 8 V rectangular pulse train with width of 0.05 ms and 1 kHz frequency were applied. Lastly, voltage of square pulse was varied from -8 V to 8 V to perform leakage test.

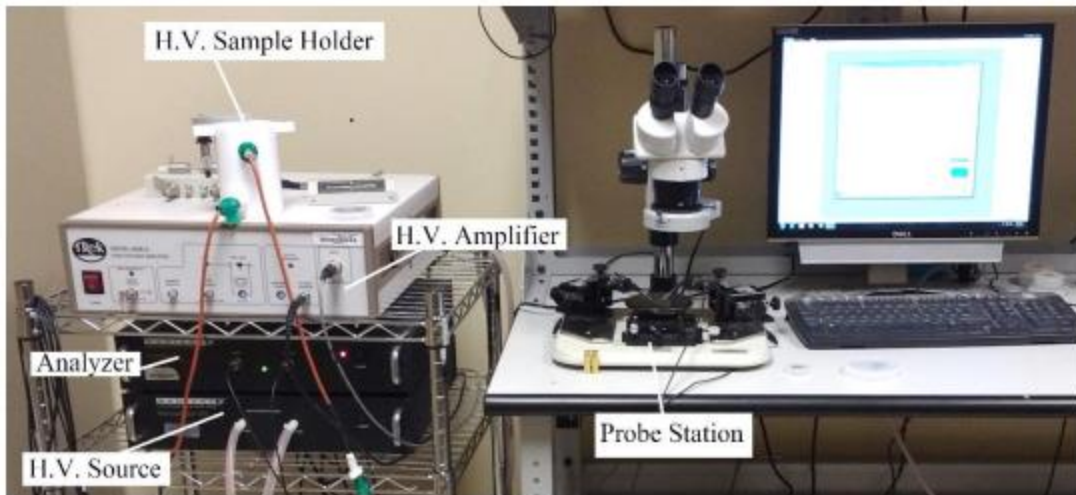


Figure 3.7: Precision LC tester, RADIANT Technologies for ferroelectric measurement.

4. GROWTH AND CHARACTERIZATION OF HfO₂-ZrO₂ NANOLAMINATE SYSTEM

4.1 Experimental

Bilayers of HfO₂-ZrO₂ were grown on Si/SiO₂/TiN by pulsed laser deposition process. The stacking structure of the sample is shown in figure 4.1. Firstly, 100 mm Si (100) wafer was oxidized in a dry oxidation furnace at 1000°C for 2 hours 30 minutes. Thickness of the oxidized Si-wafer was measured by Flimmetrics F-50 mapper and average thickness of SiO₂ obtained was 100 nm. This was followed by a deposition of 85 nm TiN on the SiO₂/Si by DC magnetron sputtering with 10 sccm argon at room temperature. Crystallinity, roughness, thickness, and sheet resistivity was measured by XRD, AFM, XRR and linear four-point probe. XRD measurements on the as-deposited TiN film show peaks of TiN (111) and TiN (200) plane at 35.5° and 41.5°, respectively as shown in figure 4.2 (a). Interestingly, these peaks of TiN shift to higher angle with the increase of temperature because of thermal stress [64]. Surface morphology of TiN depicted in figure 4.2 (b) gives roughness of 3-4nm and resistivity of TiN was measured to be 8.4-16.8 μΩ-cm which is within the reported values [65].

Two separate targets of HfO₂ and ZrO₂ were used for the deposition of HfO₂-ZrO₂ nanolaminates. Three series of samples were prepared under varying deposition conditions: thickness series, T_s (temperature) series and P_o (oxygen pressure) series. In the thickness series sample, the thicknesses of HfO₂-ZrO₂ layers were varied by controlling the number of laser pulses: for HfO₂ from 750 to 2000 pulses (5 nm-15 nm) and for ZrO₂, from 275 to 1000 pulses (5 nm-15 nm) with the substrate temperature at 750 °C and partial oxygen pressure at 0.124 mtorr. In the T_s series samples, 15 nm

HfO₂/15 nm ZrO₂ was deposited at room temperature, at 500 °C and at 750 °C with an oxygen pressure of 0.124 mtorr. In the pressure series samples, 15 nm HfO₂/15 nm ZrO₂ was deposited using an oxygen pressure of 0.124 mtorr and 10⁻⁶ torr keeping a constant substrate temperature at 750 °C. At the end of the deposition, all the samples were cooled under oxygen pressure of 10⁻⁶ torr. Structural characterization was performed by X-ray diffraction (XRD) using Cu K_α radiation and atomic force microscopy. For electrical characterization, TiN top electrodes with 50 nm thickness and 1-1.5 mm in diameter, were deposited by dc magnetron sputtering through a shadow mask. After deposition of the top electrode, the samples were annealed at 750 °C in N₂ atmosphere for 1 min for increased crystallinity. Ferroelectric polarization loops at a frequency of 1 kHz and leakage current were measured in a top–bottom configuration (grounding the bottom electrode and biasing the top one) at room temperature using a Precision LC tester as shown in figure 4.3. To obtain wake-up effects, polarization vs voltage (P-V) hysteresis loop was measured after 10⁵ cycles of 8 V bipolar rectangular pulses. For endurance test, a 1 kHz bipolar rectangular pulse train with 8 V amplitude and width of 0.05 ms was applied.

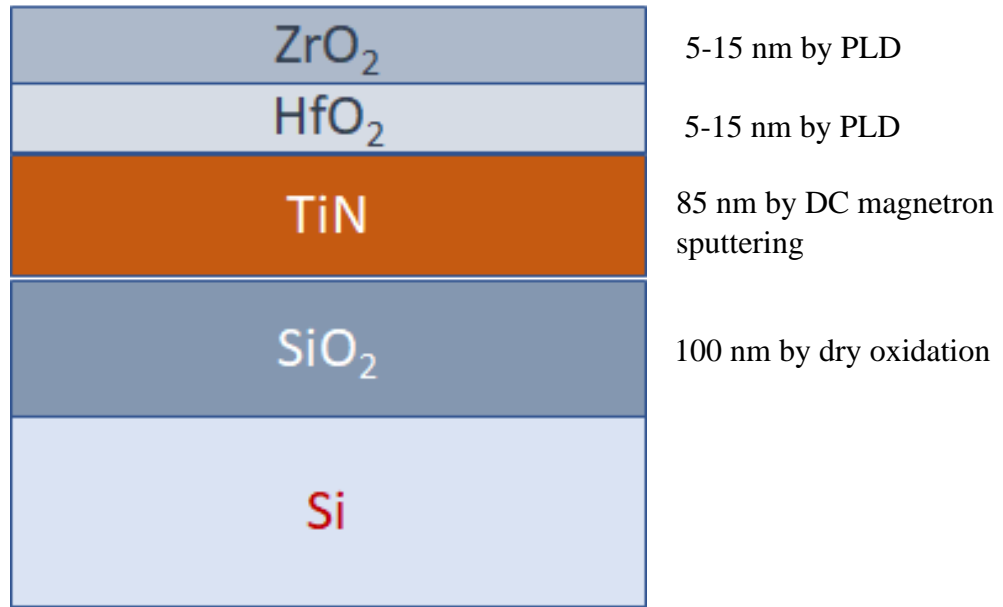


Figure 4.1: Typical bi-layer film structure used in this study.

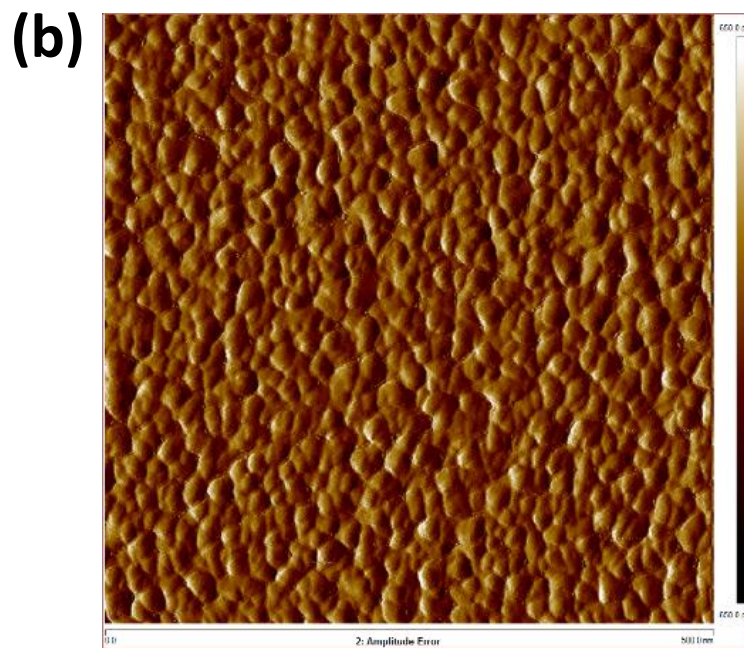
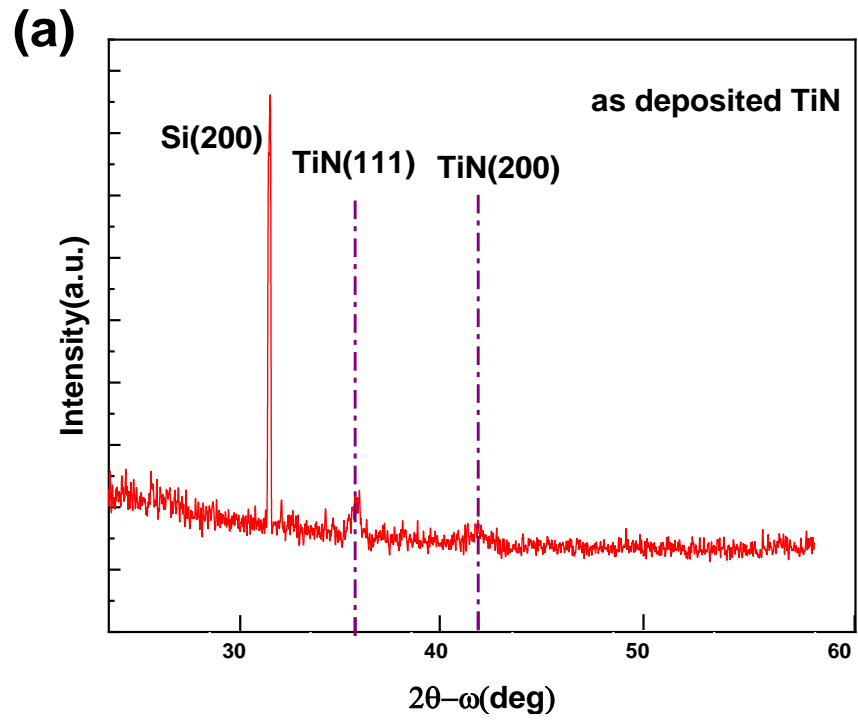


Figure 4.2: (a) XRD 2θ - ω scan of as deposited TiN, (b) AFM topological $0.5\ \mu\text{m} \times 0.5\ \mu\text{m}$ image of TiN surface.

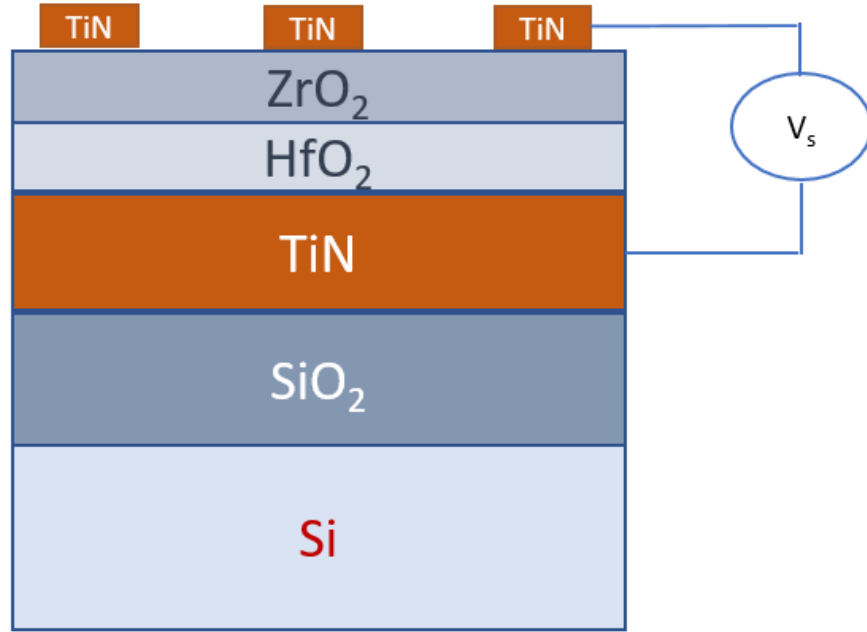


Figure 4.3: Electrical connection setup for ferroelectric measurement.

4.2 Results and Discussion

4.2.1 Structural Analysis

The effect of thickness of the individual layers on the crystallinity of HfO₂-ZrO₂ was addressed first. The XRD 2θ - ω scan in figure 4.4 shows (-111) reflection of the monoclinic HfO₂-ZrO₂ peak at $2\theta \sim 27^\circ$, (002) reflection of orthorhombic HfO₂-ZrO₂ at $2\theta \sim 35.1^\circ$ and (220) peak from m/t-reflection from nanolaminates at $2\theta \sim 48.7^\circ$, common in polycrystalline films [43]. The intensity of o (002) peak, normalized to that of the m (-111) peak, increases with layer thickness and the o (002) peak becomes narrower and more intense as shown in figure 4.5(a-c), indication of improved crystallinity in thicker films. Besides, the interplanar spacing (d), which is defined as the distance between two parallel planes of crystal of diffraction angle (002) also decreases with increasing thickness, denoting the increasing contraction in the film with thicknesses. In case of

single layer 15 nm HfO₂, the interplanar spacing $d(002) \sim 2.558 \text{ \AA}$ which is greater than that obtained from the 10 nm HfO₂/10 nm ZrO₂ and the 5 nm HfO₂/5 nm ZrO₂ structures. This is because of the absence of top ZrO₂ layer which is responsible for the mechanical stress to the HfO₂ layer. With increasing ZrO₂ layer thickness, the degree of rigidity and confinement increases and stabilizes the high-pressure ferroelectric o-phase in the film [42], [43]. On the other hand, a single layer of 15 nm ZrO₂ shows a small peak at 34.8° which corresponds to (002) peak of the monoclinic phase. ZrO₂ has a higher degree of crystallization and it favors monoclinic/tetragonal phase after crystallization [43], [66].

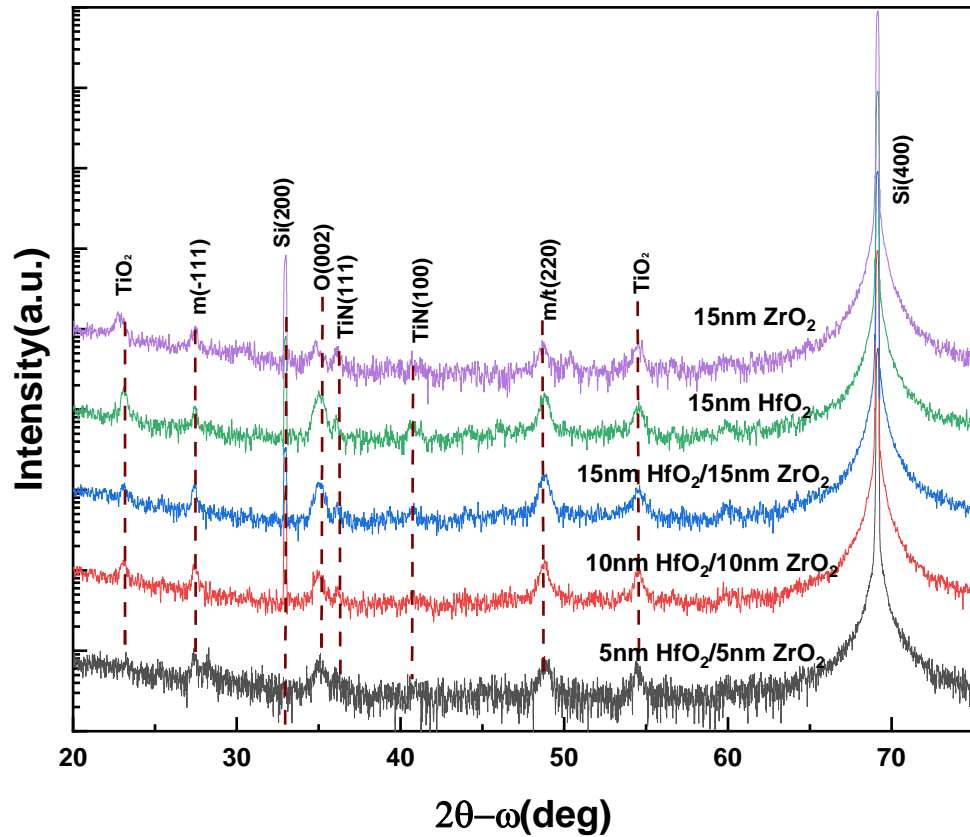


Figure 4.4: XRD $2\theta - \omega$ scan of HfO₂-ZrO₂ deposited at 750 °C and $P_0=0.124$ mtorr with different thicknesses.

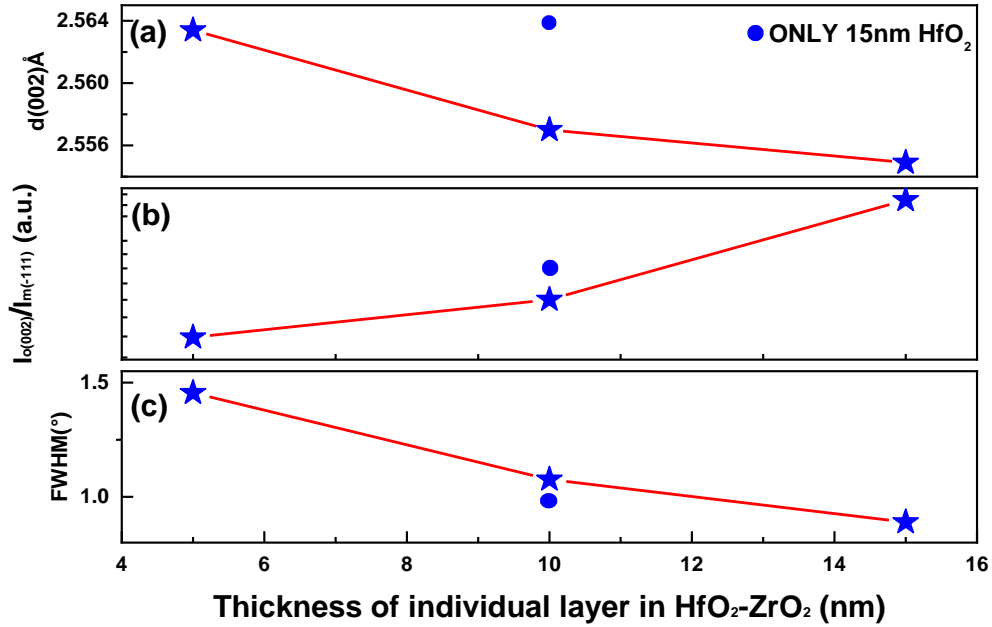


Figure 4.5: (a) Interplanar spacing of o (002), (b) Normalized intensity of o (002) peak w.r.t m (-111) and (c) FWHM with varying thickness.

To confirm the role of the ZrO₂-layer further, a 15 nm ZrO₂ was deposited as the starting layer as shown in figure 4.6 (15 nm ZrO₂/15 nm HfO₂) and compared with 15 nm HfO₂/15 nm ZrO₂ structure in which the ZrO₂ is top layer. The XRD 2θ-ω scan, in figure 4.7, shows that the ZrO₂ starting structure has two dominant monoclinic phases of m (-111), m (111) at 28.22° and 31.52°, respectively, and one broad peak representing the orthorhombic o (002) phase. This is because, ZrO₂ crystallizes before the crystallization of the HfO₂-top layer and creates a tensile stress on the HfO₂ layer. As a result of this tensile stress, the activation energy barrier between m-phase and t-phase, and critical radius of m-phase decreases which increases the nucleation rate of the monoclinic phase in the film [42]. The normalized higher intensity ratio of o (002) / m (-111) + m (111) also confirms the higher crystallinity of o-phase in the HfO₂-starting structure as shown in figure 4.8.

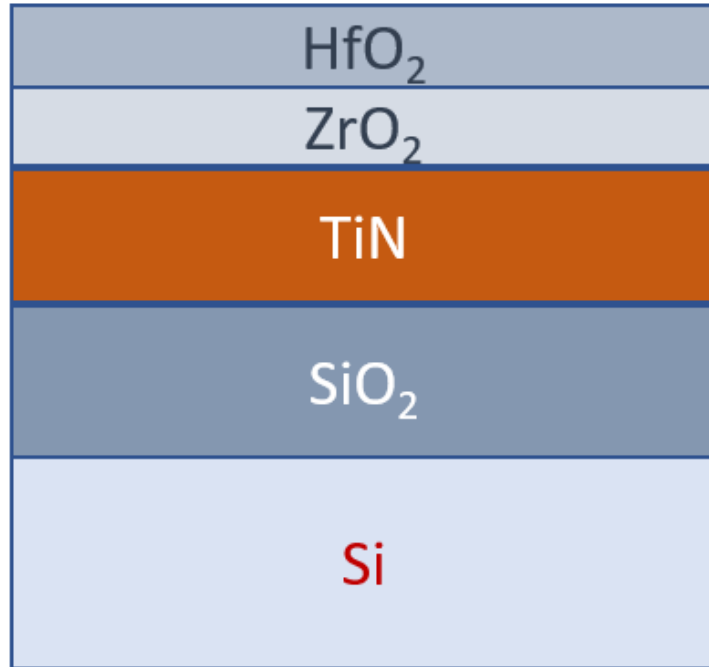


Figure 4.6: Stacking sequence of 15 nm ZrO_2 / 15 nm HfO_2 where 15 nm ZrO_2 is starting layer.

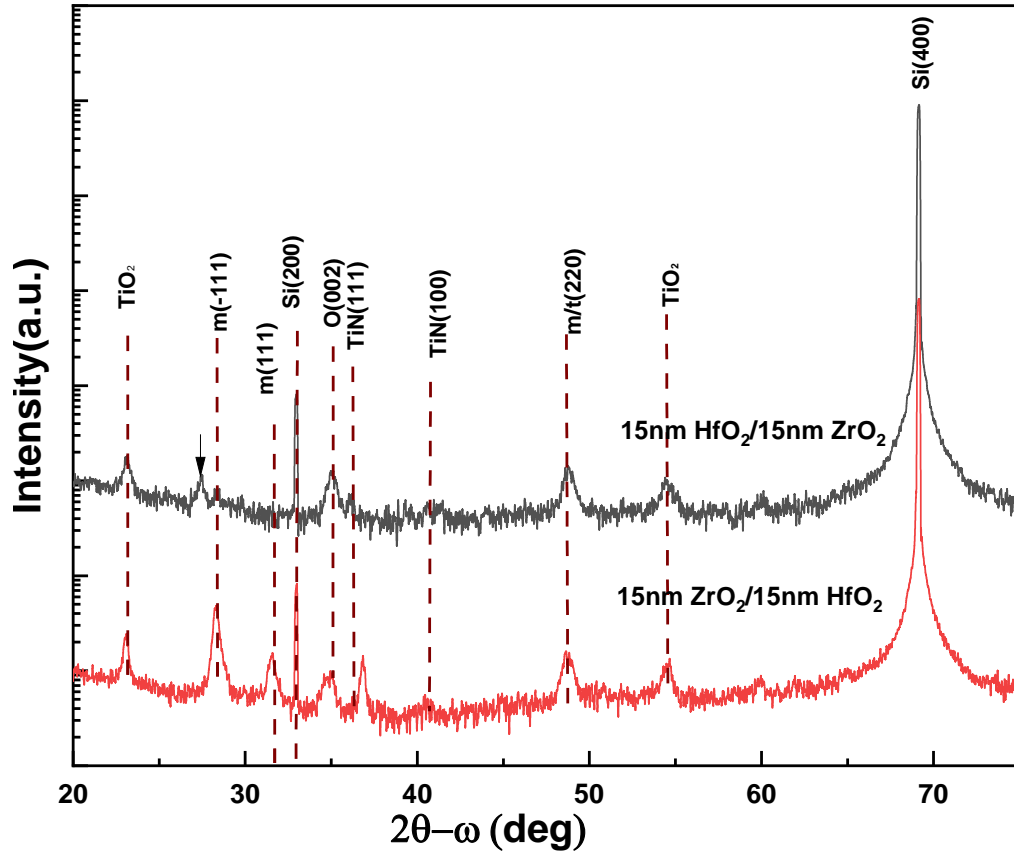


Figure 4.7: XRD 2θ - ω scan of HfO₂ starting sample (15 nm HfO₂/15 nm ZrO₂) and ZrO₂ starting layer (15 nm ZrO₂/15 nm HfO₂) after deposited at 750 °C and P₀=0.124 mtorr.

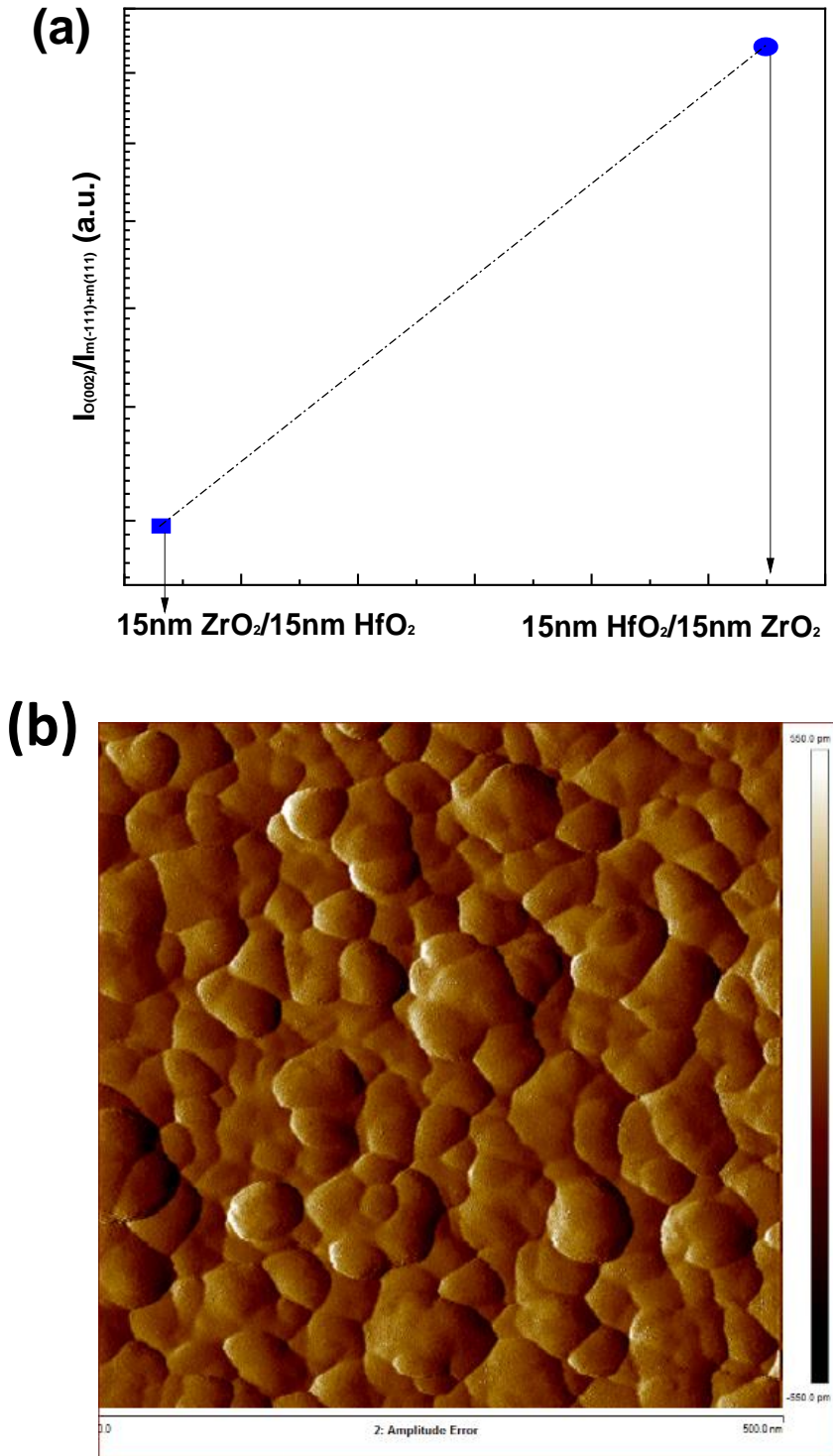


Figure 4.8: (a) Comparison of intensity of o (002) phase between ZrO_2 starting and HfO_2 starting samples, (b) AFM topographical $0.5 \mu m \times 0.5 \mu m$ image of ZrO_2 starting sample (grain size~ 43 nm).

From above analysis, it is clear that 15 nm HfO₂/15 nm ZrO₂ structure (HfO₂ as starting layer) gives the best result and so, further variation in the growth parameters will be carried out without changing the thickness and stack sequence. Figure 4.9 summarizes the effect of oxygen pressure for the 15 nm HfO₂/15 nm ZrO₂ sample on the crystallinity. Mostly monoclinic peaks and a small broad o (002) peak is present in the low pressure (P_o=10⁻⁶ torr) sample, whereas the sample deposited at higher oxygen pressure (P_o= 0.124 mtorr) showed a dominant orthorhombic phase. In the case of low-pressure sample, sufficient oxygen was not present in the growth environment during deposition resulting in an oxygen-deficient sample. Because of oxygen deficiency in HfO₂ and ZrO₂ structure, ZrO₂ could not provide enough mechanical confinement on the underlying HfO₂ layer and thus nucleation of m-phase is increased substantially. Besides, the o (002) peak slightly shifts toward a smaller angle with decreasing oxygen pressure, resulting in an increase of the interplanar spacing of o (002) and an increase in the monoclinic phase in structure. Similar behavior was also observed in another study [4].

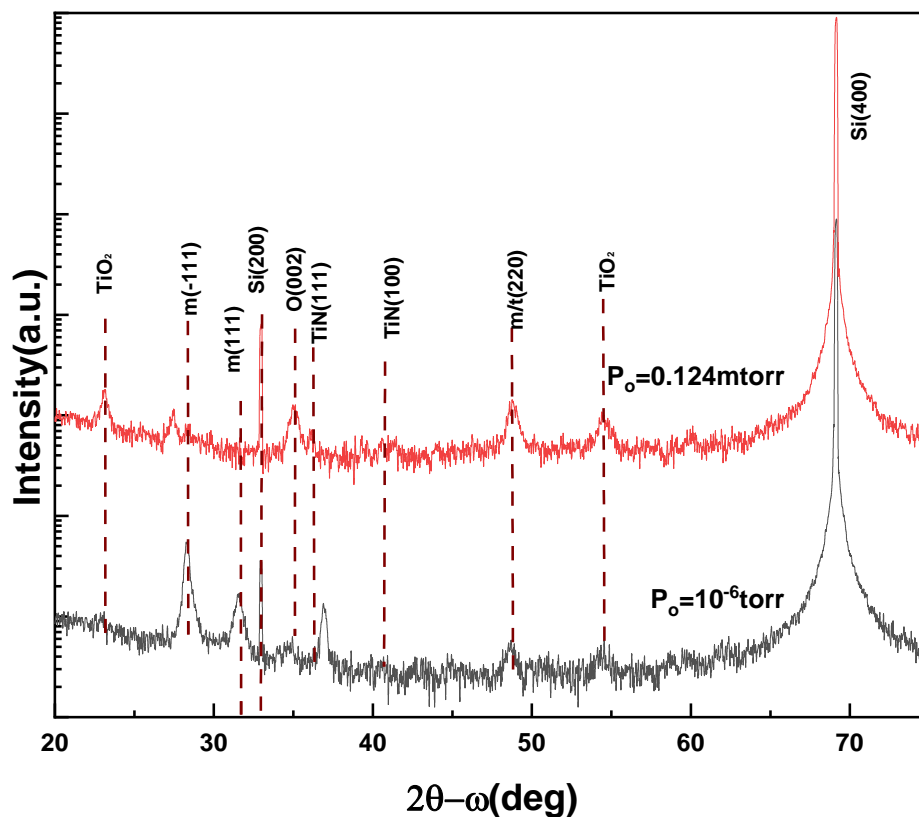
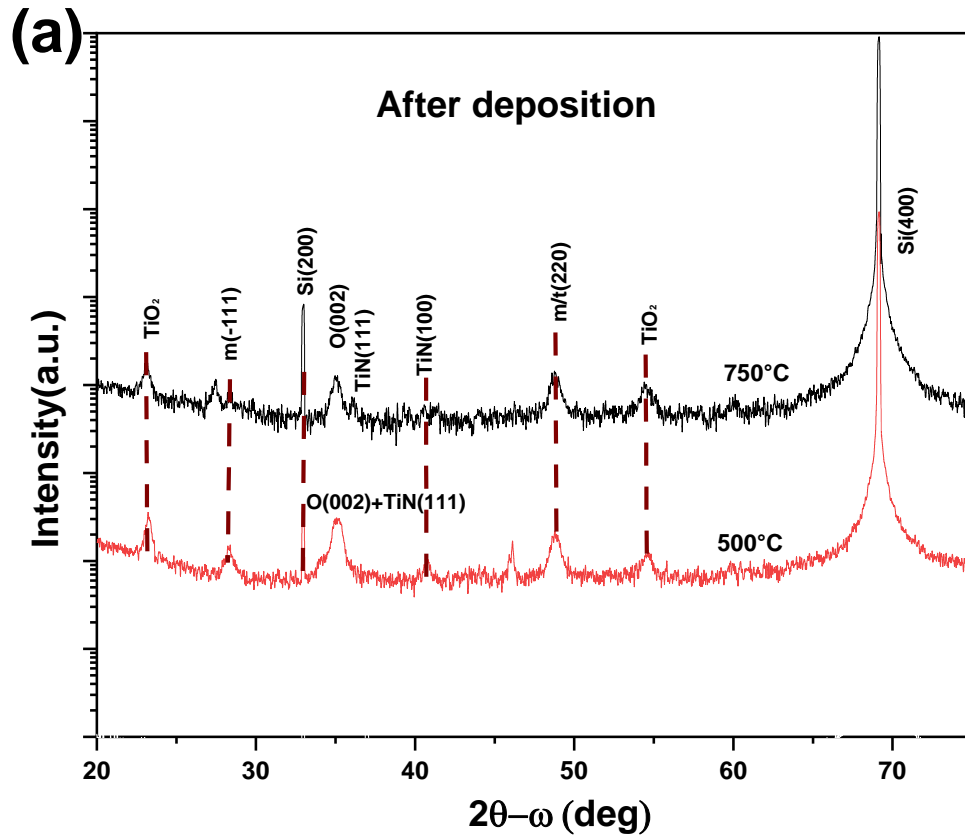


Figure 4.9: XRD 2θ - ω scans of 15 nm HfO_2 /15 nm ZrO_2 after deposited at 750 °C using oxygen pressures of 0.124 mtorr and 10^{-6} torr.

The XRD 2θ - ω scans of the 15 nm HfO_2 /15 nm ZrO_2 deposited at 750 °C, 500 °C and room temperature with pressure of 0.124 mtorr are presented in figure 4.10. It was mentioned earlier that the as-deposited TiN (111) peak is present at 35-35.5° and shifts to the right with increasing temperature because of thermal stress in the structure. For 750°C, TiN (111) peak created a shoulder peak close to o (002) peak. But, for the 500°C deposition, it is hard to distinguish the o (002) phase of the film and TiN (111) peak separately as shown in figure 4.10(a). The sample that deposited at 500 °C showed distinguishable the peaks of film and TiN after annealing at 750°C in N_2 atmosphere for 1 min. A higher amount of monoclinic phase is present in the film as shown in figure

4.10(b). This is because ZrO_2 has lower crystallization temperature than HfO_2 and so, at $500^\circ C$, ZrO_2 crystallizes first and favors m-phase in its structure. Therefore, HfO_2 also followed the same crystallization behavior as ZrO_2 even after annealing. The film deposited at room temperature and was annealed at N_2 atmosphere for 1min at $700^\circ C$ remains amorphous even after annealing.



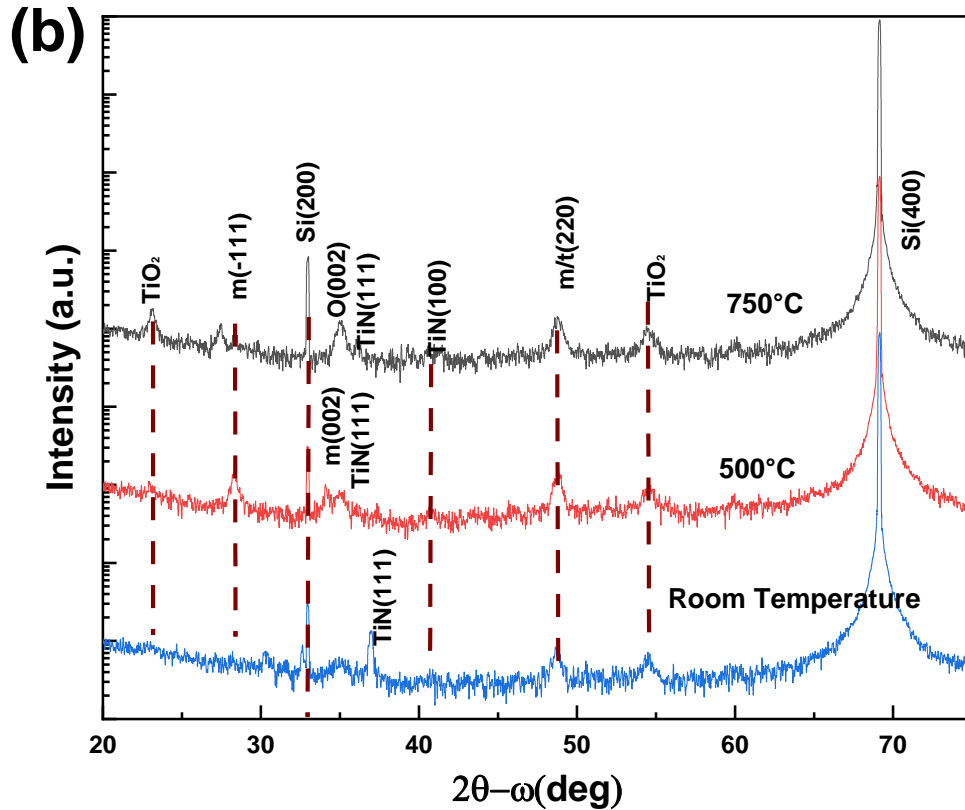


Figure 4.10: XRD 2θ - ω scans of 15 nm $\text{HfO}_2/15\text{ nm ZrO}_2$ deposited at $P_0= 0.124\text{ mtorr}$ with different temperatures (a) after deposition and (b) after annealing at N_2 atmosphere for 1min.

Lastly, 3-pairs of HfO_2 - ZrO_2 layer were deposited, each of which was 5 nm thick, to analyze the effect of the superlattice structure as shown in figure 4.11. The XRD 2θ - ω in figure 4.12 shows similar spectrum as a 5 nm $\text{HfO}_2/5\text{ nm ZrO}_2$ bilayer film (Figure 4.4). No improvement in crystallinity towards the o [002] was visible for the superlattice structure. This could be due to thinner ZrO_2 layer and it could not provide enough contraction on HfO_2 layer [42], [43].

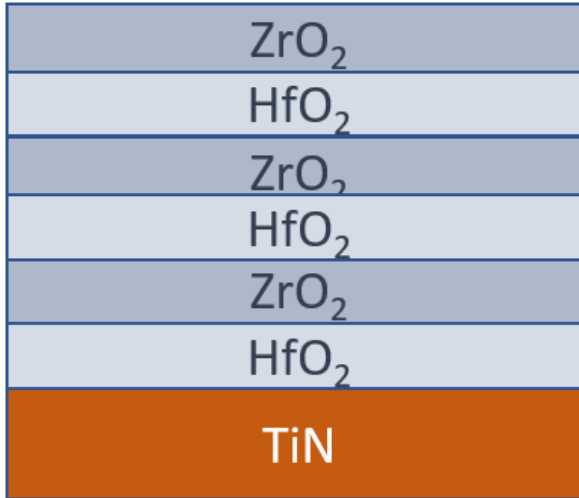


Figure 4.11: Superlattice structure (5nm HfO₂/5 nm ZrO₂) x3.

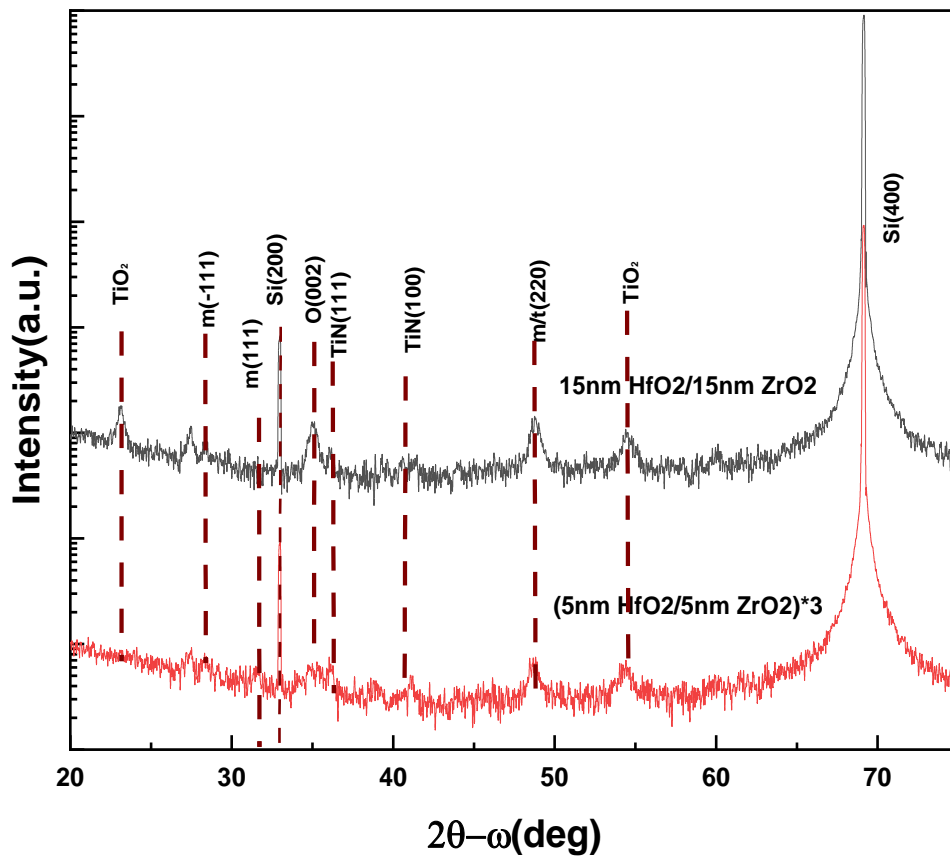
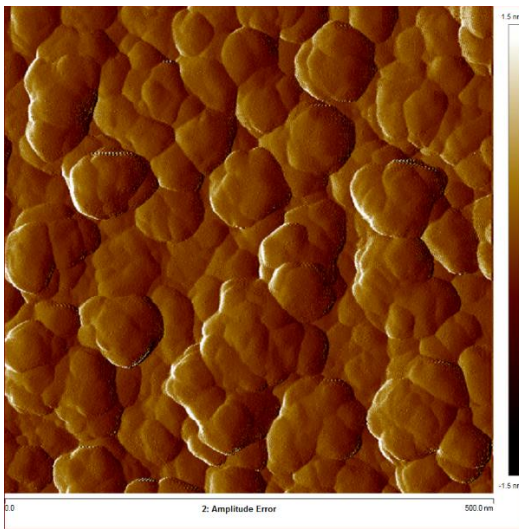
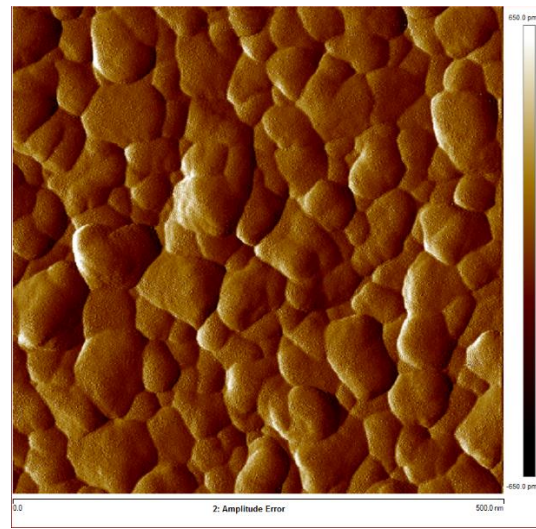


Figure 4.12: XRD 2θ - ω scans of superlattice structure (5 nm HfO₂/5 nm ZrO₂) x3.

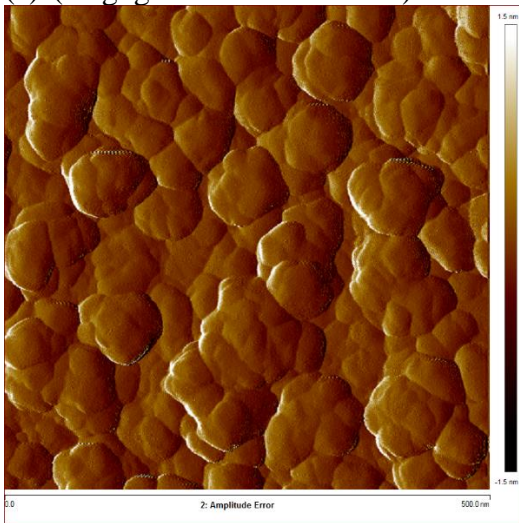
Figure 4.13 shows the influence of the deposition conditions on surface morphology. In thickness series sample, average grain size increases from 38.46 nm to 55.55 nm with increasing thickness. This is attributed to the longer thermal budget for thicker film than thinner during deposition. In the temperature and oxygen pressure series samples, the sample deposited at lower temperature and pressure showed much smaller grain size and leakage current than the samples grown at higher temperature and pressure.



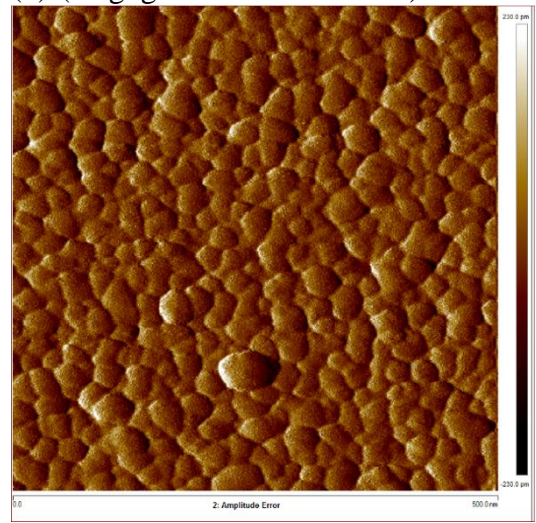
(a) (Avg. grain Size=55.55 nm)



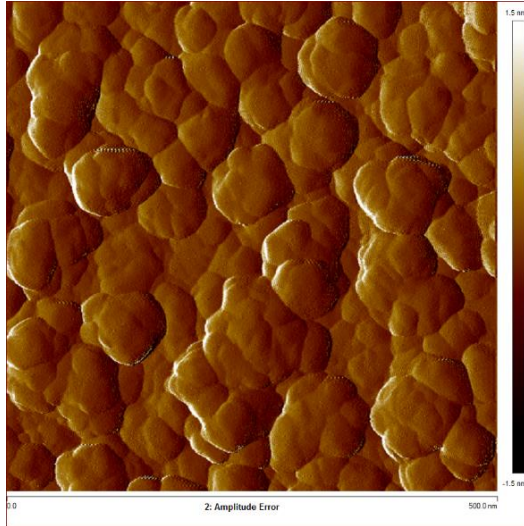
(b) (Avg. grain Size=40.36 nm)



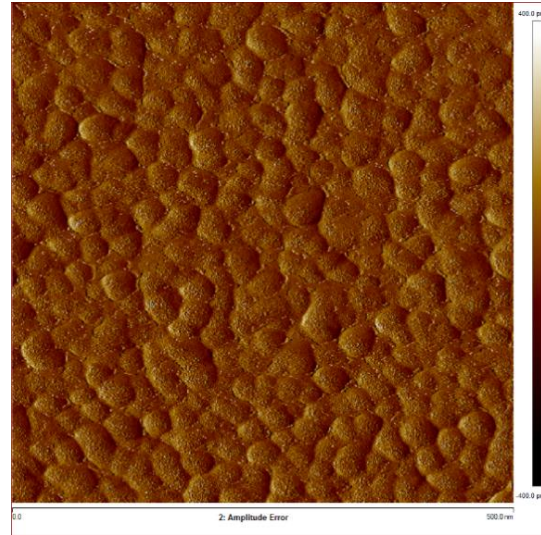
(c) Avg. grain Size=55.55 nm)



(d) (Avg. grain Size=24 nm)



(e) (Avg. grain Size=55.55 nm)



(f) (Avg. grain Size=29.41 nm)

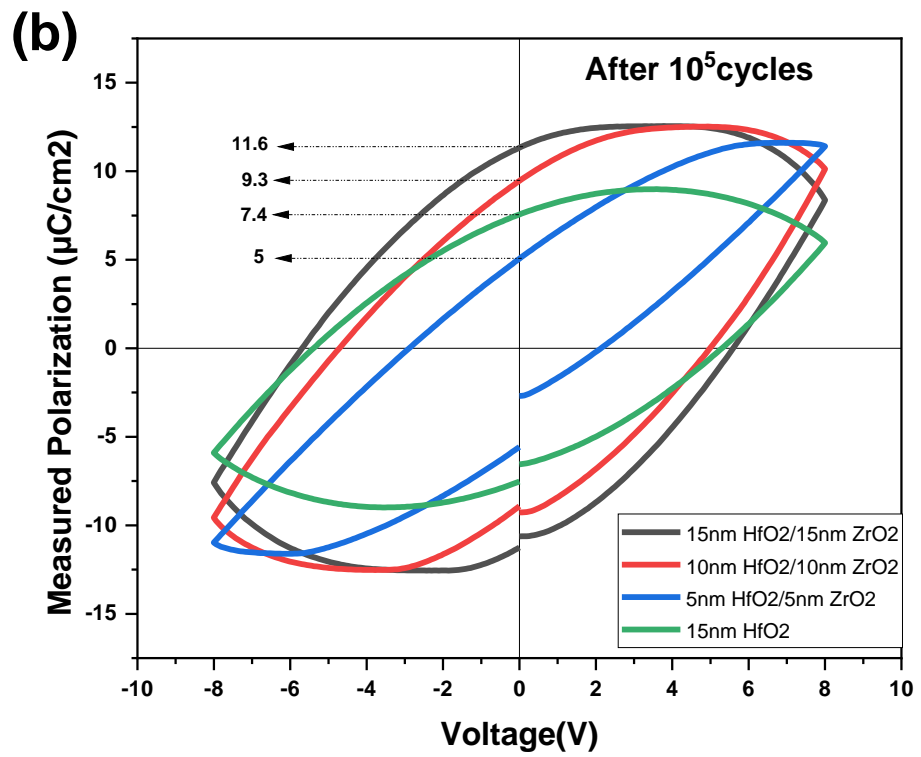
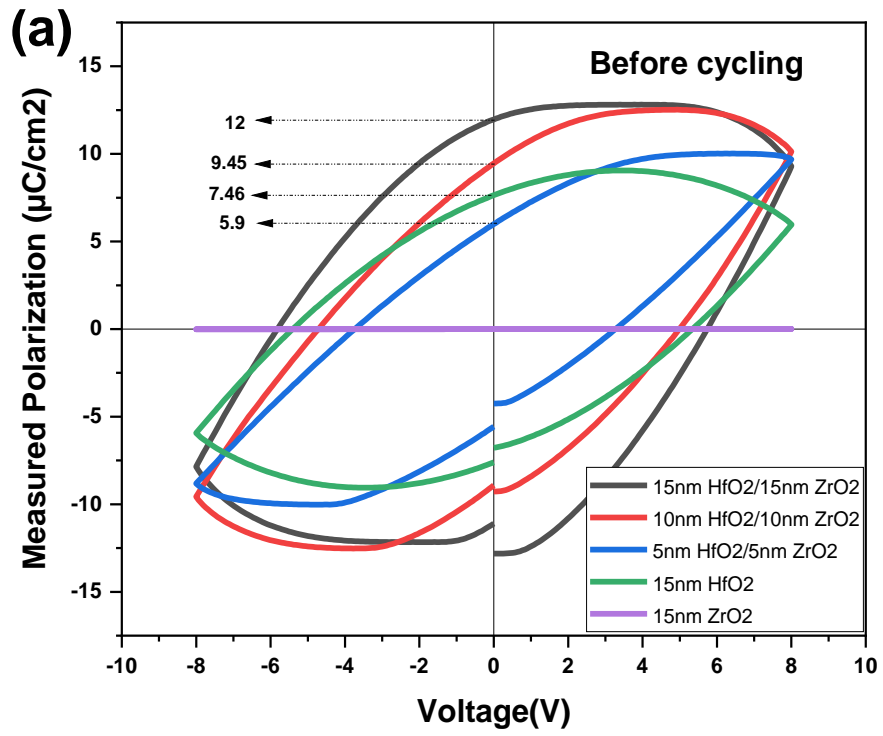
Figure 4.13: AFM topological $0.5 \mu\text{m} \times 0.5 \mu\text{m}$ images of $\text{HfO}_2\text{-ZrO}_2$ samples at different deposition conditions. Thickness series: (a) 15 nm $\text{HfO}_2/15 \text{ nm ZrO}_2$ and (b) 5nm $\text{HfO}_2/5 \text{ nm ZrO}_2$ deposited at $P_0=0.124 \text{ mtorr}$ and $T = 750 \text{ }^\circ\text{C}$, temperature series: 15 nm $\text{HfO}_2/15 \text{ nm ZrO}_2$ deposited at $P_0=0.124 \text{ mtorr}$ with temperature of (c) $750 \text{ }^\circ\text{C}$ (d) $500 \text{ }^\circ\text{C}$, pressure series: 15 nm $\text{HfO}_2/15 \text{ nm ZrO}_2$ deposited at $750 \text{ }^\circ\text{C}$ with pressure of (e) 0.124 mtorr and (f) 10^{-6} torr .

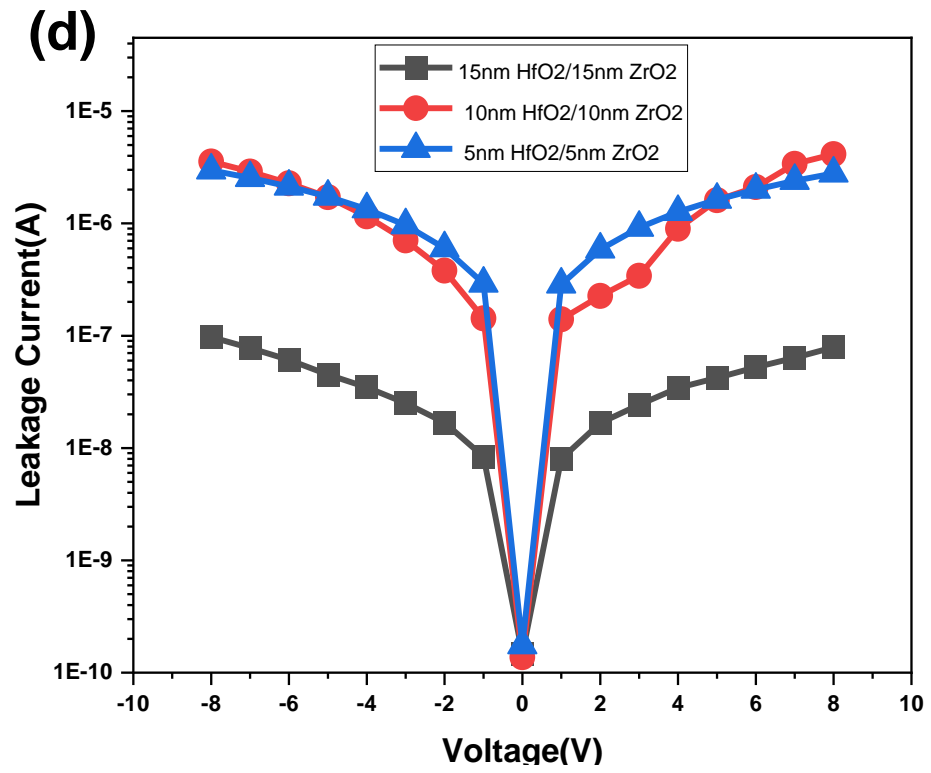
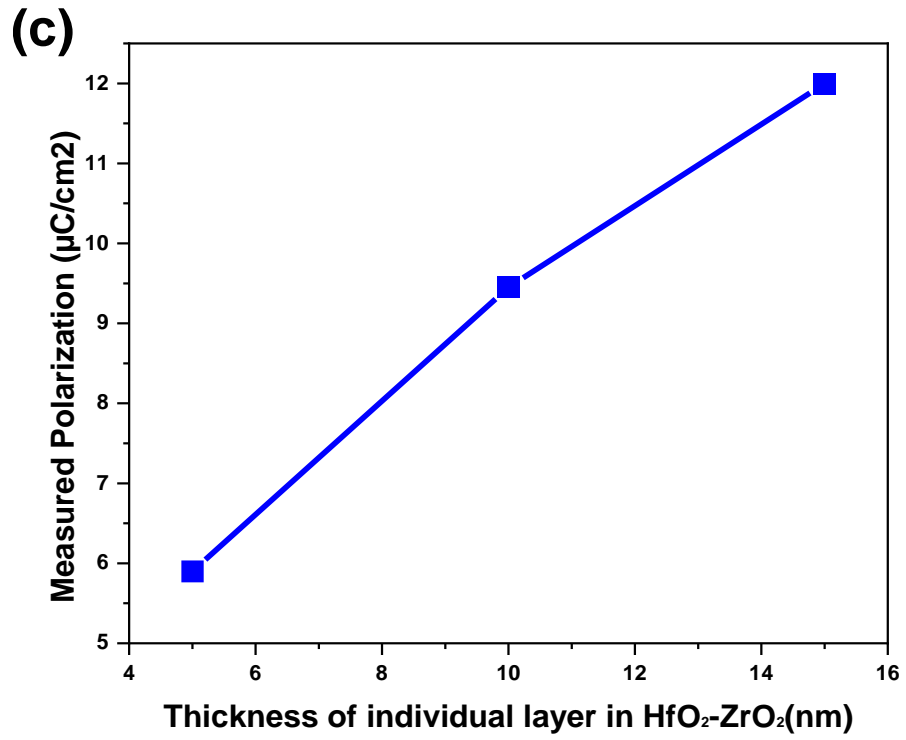
4.2.2 Electrical Characterization

Ferroelectric polarization loops for thickness series films are shown in figure 4.14. Polarization vs voltage (P-V) hysteresis curve shows significant amount of remnant polarization in all samples except the single layer of ZrO_2 . To obtain the wake-up effects, polarization was measured again after 10^5 cycling as shown figure 4.14 (b). No wake-up effects were observed in the samples which confirms the fully oxidized films, and no defects are present in the structure. Wake-up effects refer to the increase in the remnant polarization with increasing electric field cycling. Oxygen vacancies and defects redistribute evenly throughout the films which increases the o-phase fraction and so, polarization increases. In case of ALD, the samples deposited at lower than $300 \text{ }^\circ\text{C}$ and

oxygen vacancies were present in the film. Those samples showed wake-up up to 10^4 - 10^5 cycles to get the highest remnant polarization. In this study, high temperature as well as high oxygen pressure was used during deposition and so, it was possible to grow fully oxidized film.

The remnant polarization increases with the thickness of individual layer in nanolaminates as the crystallinity of orthorhombic (002) phase fraction increases over monoclinic phase. The thickness dependence of polarization for different thicknesses of HfO₂-ZrO₂ nanolaminates is shown in figure 4.14(c). Remarkably, the single layer of 15 nm HfO₂ shows a remnant polarization of $7.46 \mu\text{C}/\text{cm}^2$ but the hysteresis loop could not saturate perfectly. This might be due to the absence of ZrO₂ top layer, which exhibits mechanical stress, resulting in lower amount of o (002) phase fraction. The leakage current at different applied voltages was measured and is shown in figure 4.14(d). It is seen that leakage current increases with decreasing thickness which attributed to grain size in the films and lower grain size increased the leakage current. The thicker film shows a considerably low leakage current of 10^{-7}A at 8V. Figure 4.14(e) shows the endurance behavior of thickness series films up to 10^8 cycles. Polarization in thicker samples did not change up to 10^8 cycles but thinner films showed some abrupt changes up to 10^5 pulses as shown in figure 4.14(f). This might be due to the defects generated in the thinner films during cycling and redistributed evenly onwards.





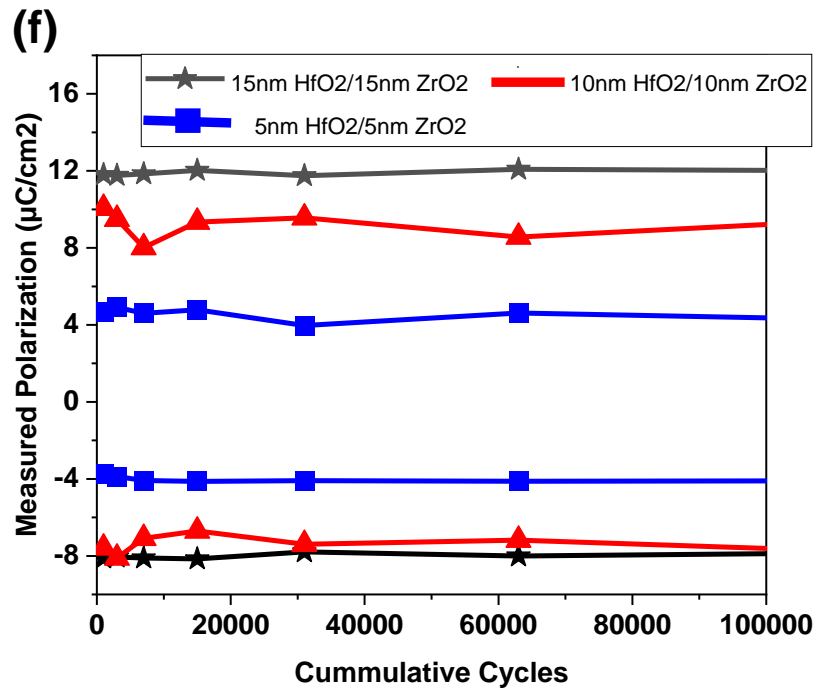
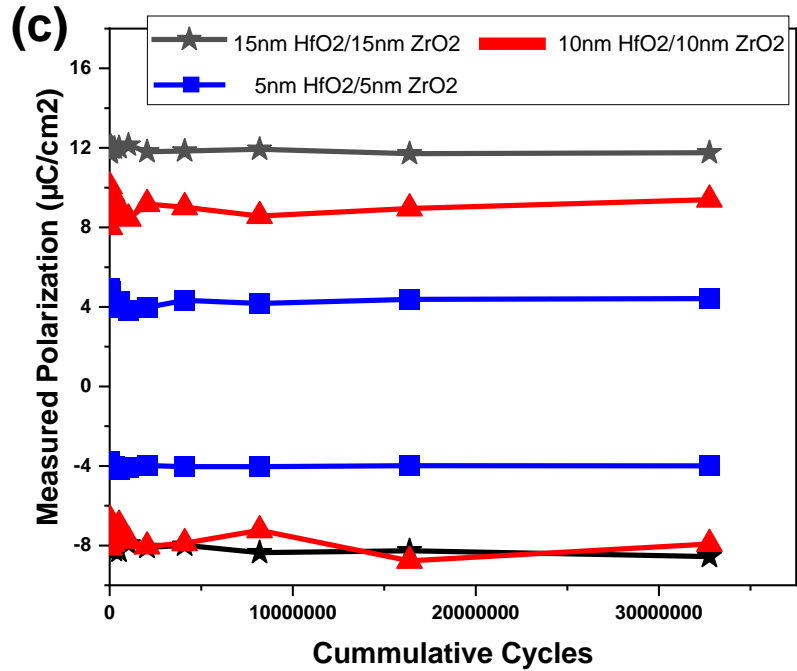
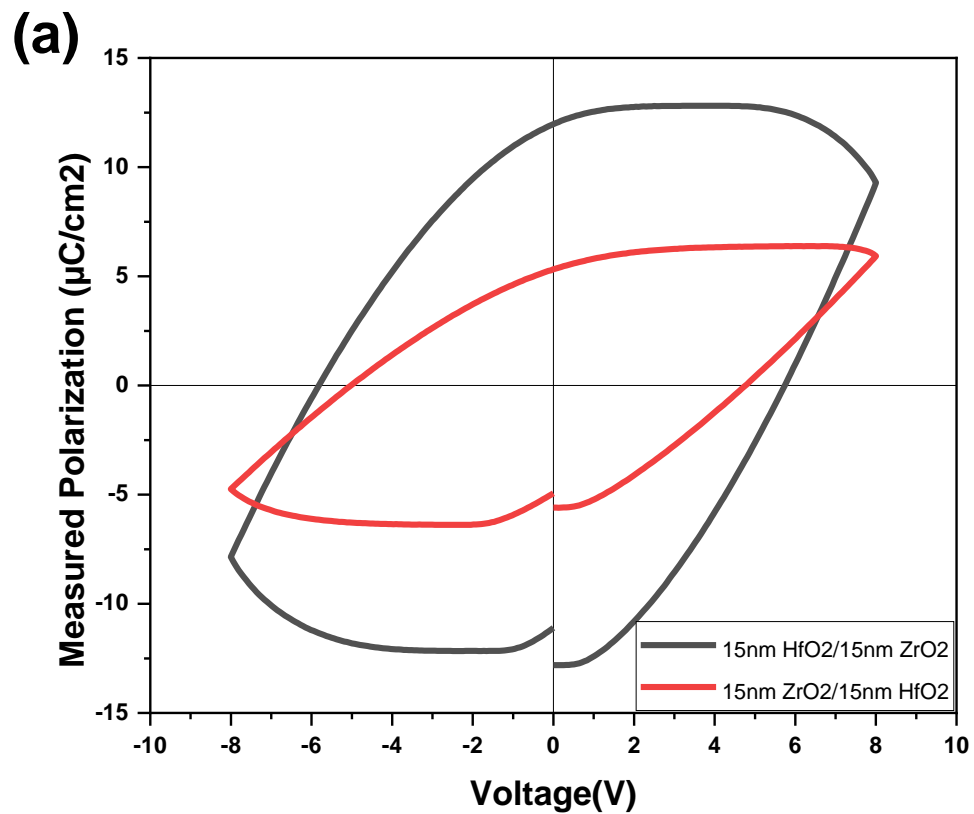


Figure 4.14: Ferroelectric measurement: (a) P-V hysteresis loop before field cycling, (b) P-V hysteresis loop after 10^5 field cycling, (c) Thickness dependence polarization trend, (d) Leakage test with varying thickness, (e) Endurance test, (f) Endurance up to 10^5 cycles.

Ferroelectric measurement, leakage, and endurance of altered sequence structure (15 nm ZrO₂/15 nm HfO₂) are shown in figure 4.15(a-b) and compared with 15 nm HfO₂/15 nm ZrO₂. Remnant polarization is lower in the ZrO₂-starting sample than in the HfO₂-starting sample as m-phase is dominant in the film that has the ZrO₂ as the starting layer. Besides, ZrO₂-starting sample shows higher leakage current because of lower grain size in the film.



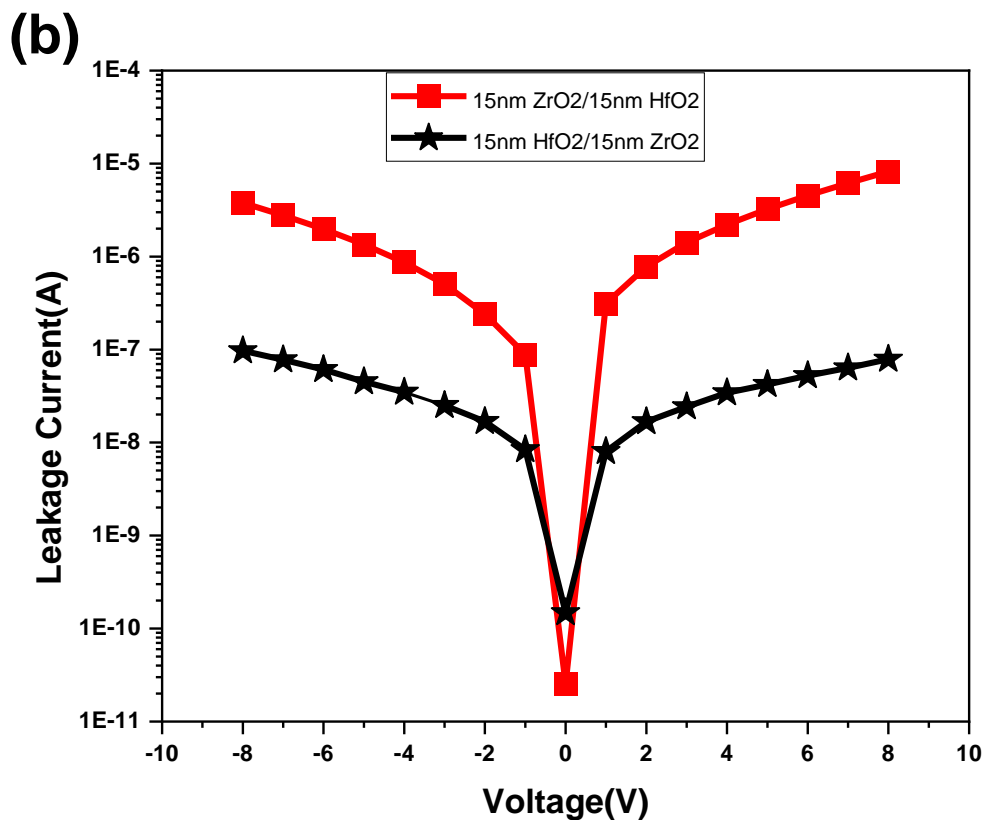


Figure 4.15: Ferroelectric measurement: (a) P-V hysteresis loop, (b) Leakage test for ZrO₂ starting sample and HfO₂ starting sample.

Ferroelectric test measurement of the P_o series and T_s series are shown in figure 4.16(a-b). The samples deposited at low pressure and room temperature did not exhibit hysteresis behavior in the P-E test. Leakage current increases with decreasing pressure and temperature because of low grain size in the crystal as shown in figure 4.17(b). Ferroelectric measurement of sample grown at 500 °C showed an oval-shape response indicative of an ideal resistor as shown in figure 4.17(a) which is due to the high leakage current (figure 4.17(b)) corresponding to lower grain size in the film.

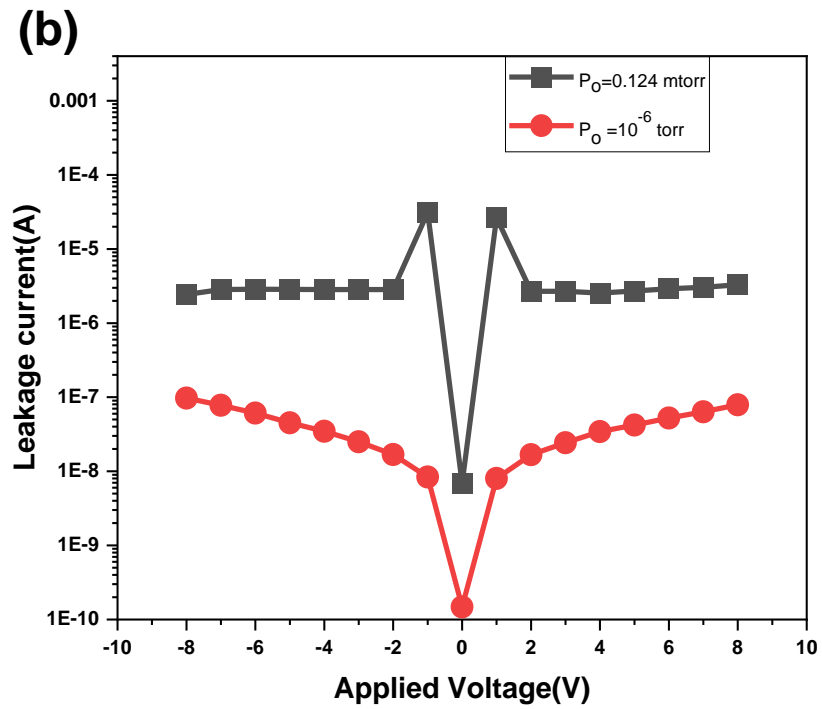
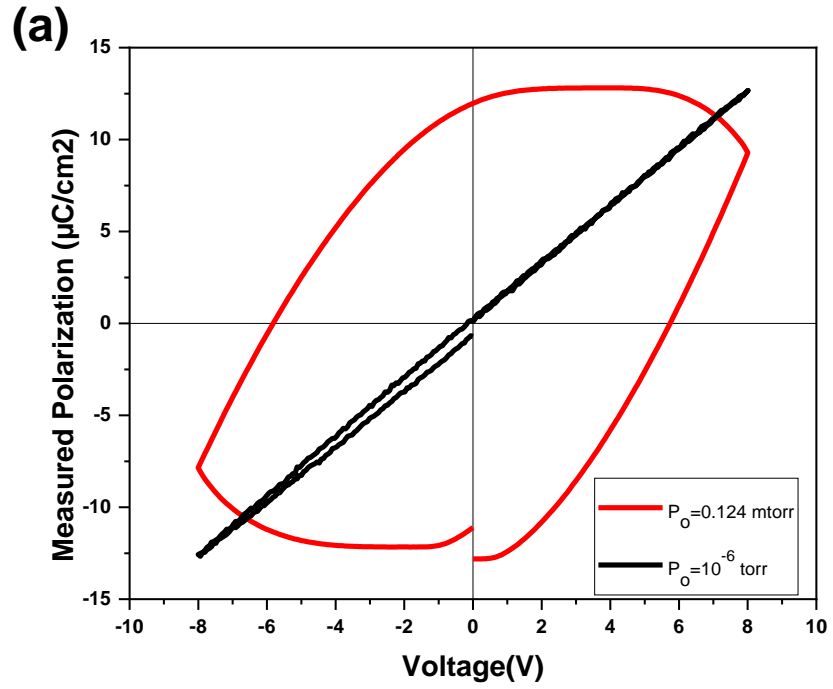


Figure 4.16: Ferroelectric measurement for 15 nm HfO_2 /15 nm ZrO_2 deposited at 750°C with different oxygen pressure.

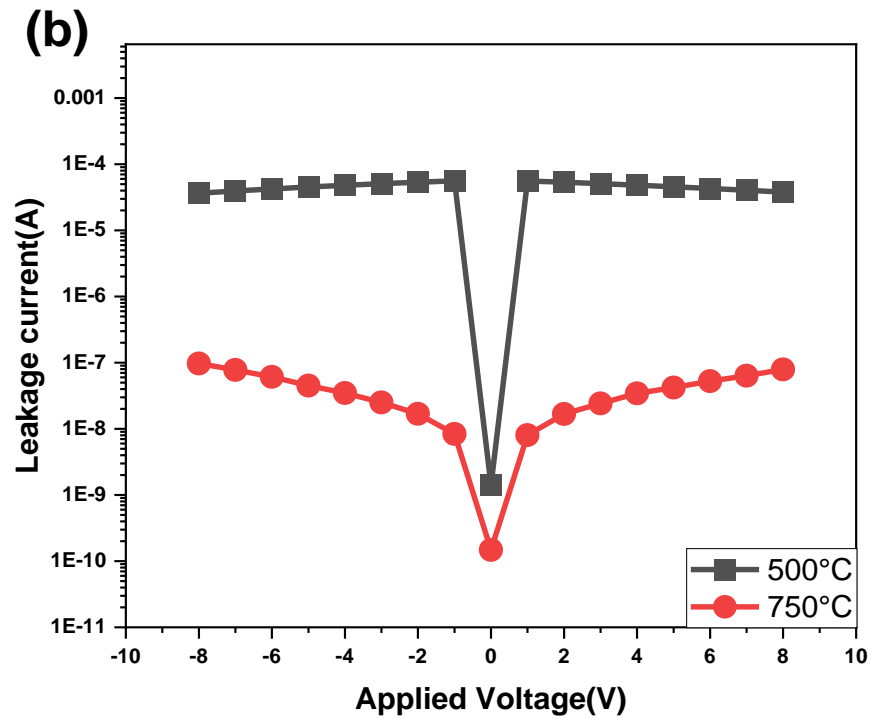
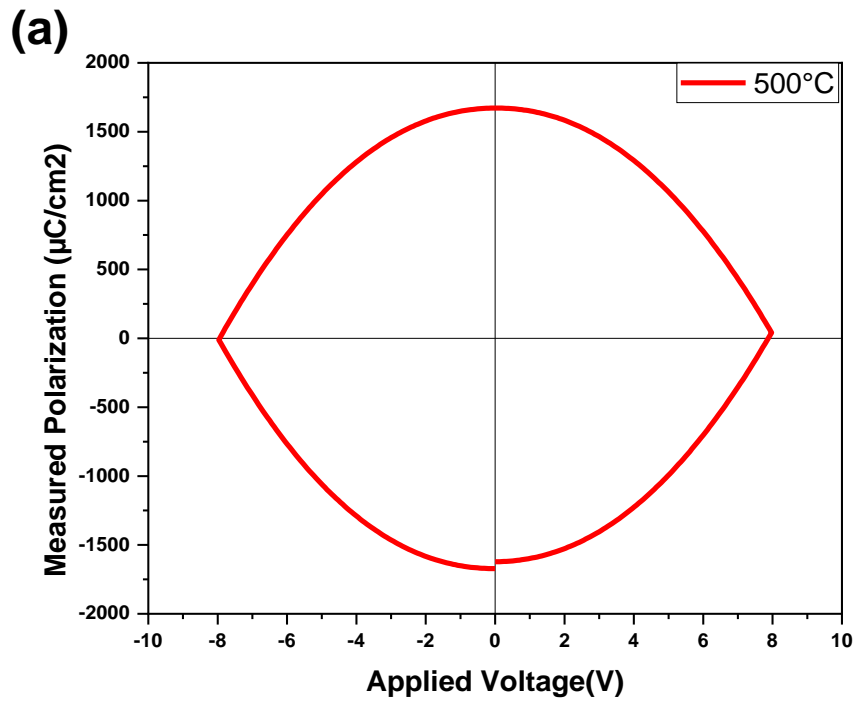


Figure 4.17: Ferroelectric measurement for 15 nm $\text{HfO}_2/15$ nm ZrO_2 (a) P-V hysteresis loop when deposited at 500 °C (b) Leakage current for 15 nm $\text{HfO}_2/15$ nm ZrO_2 at 500°C and 750 °C.

Hysteresis behavior of the superlattice structure is shown in figure 4.18. The remnant polarization is significantly reduced in comparison to the 15 nm HfO₂ /15 nm ZrO₂ (12 $\mu\text{C}/\text{cm}^2$) or the 5 nm HfO₂/5 nm ZrO₂ (5 $\mu\text{C}/\text{cm}^2$) bilayer films because of higher amount of monoclinic phase in the structure.

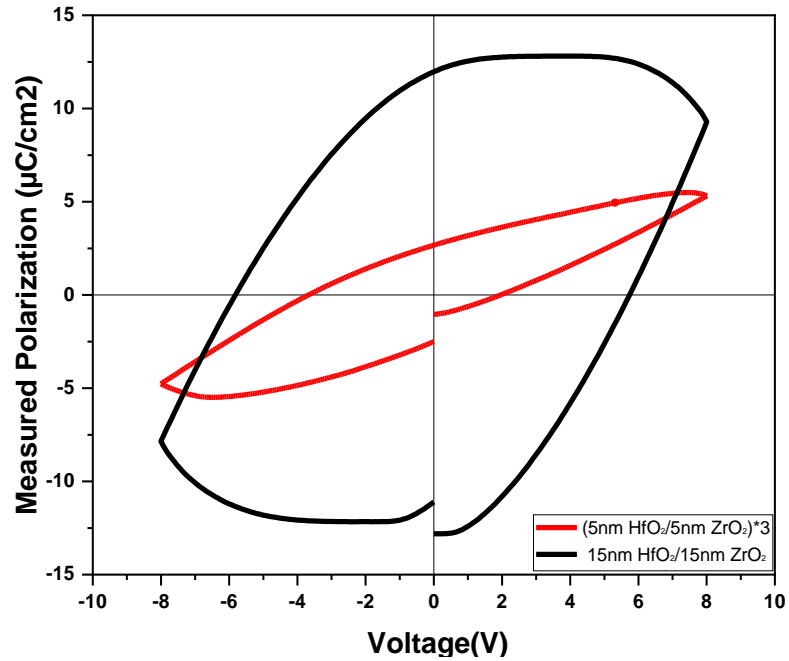


Figure 4.18: Ferroelectric measurement for superlattice structure (5 nm HfO₂/5 nm ZrO₂) x3.

Figure 4.19 summarizes the effects of thickness, temperature, and oxygen pressure on the crystalline phases and the remnant polarization. The intensity of the o (002) phase as well as remnant polarization increases with increasing thickness, pressure and temperature. A comparative study with this work is shown in figure 4.20 which summarizes the thickness dependence polarization and endurance for HfO₂-based structures with various dopants. By taking the 10⁵ wake-up cycles into account, the HfO₂-ZrO₂ nanolaminates structure of this work showed endurance > 10¹² cycles with remnant

polarization of $12 \mu\text{C}/\text{cm}^2$ for the thicker samples and $5 \mu\text{C}/\text{cm}^2$ in the thinner sample. The remnant polarization of these structures used in this study is smaller than that reported for the Gd doped HfO_2 but the Gd doped HfO_2 endurance is 10^5 - 10^7 cycles which significantly lower than this work. While ALD grown $4 \text{ nm HfO}_2/4 \text{ nm ZrO}_2$ showed higher remnant of $17 \mu\text{C}/\text{cm}^2$ whereas the $5 \text{ nm HfO}_2/5 \text{ nm ZrO}_2$ grown by PLD showed only $5 \mu\text{C}/\text{cm}^2$ but in case of endurance, the PLD grown $5 \text{ nm HfO}_2/5 \text{ nm ZrO}_2$ is higher than ALD grown HfO_2 - ZrO_2 nanolaminates. Therefore, PLD grown HfO_2 - ZrO_2 nanolaminates can be promising candidates for memory applications based on their strong endurance properties.

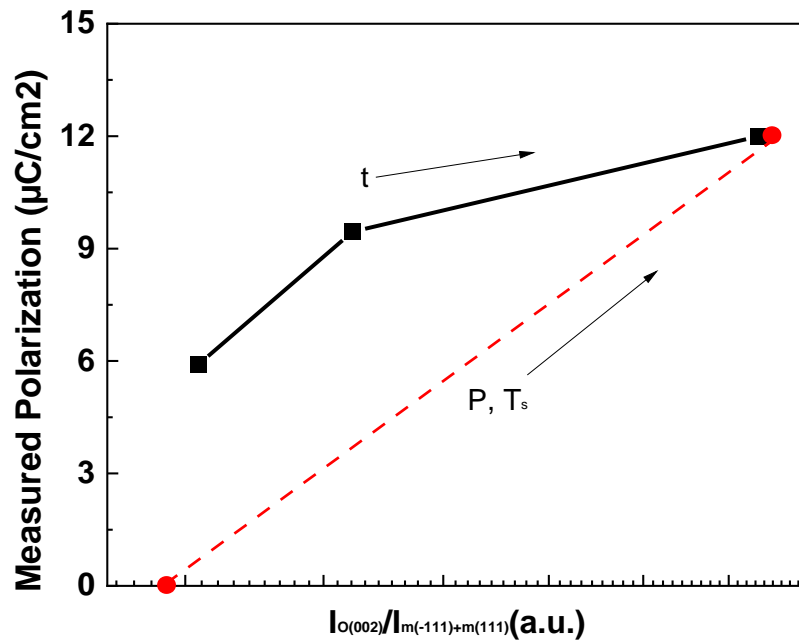


Figure 4.19: Summary of the effects of different growth conditions (thickness, temperature, and pressure) in terms of remnant polarization and intensity of o (002) w.r.t m-phases.

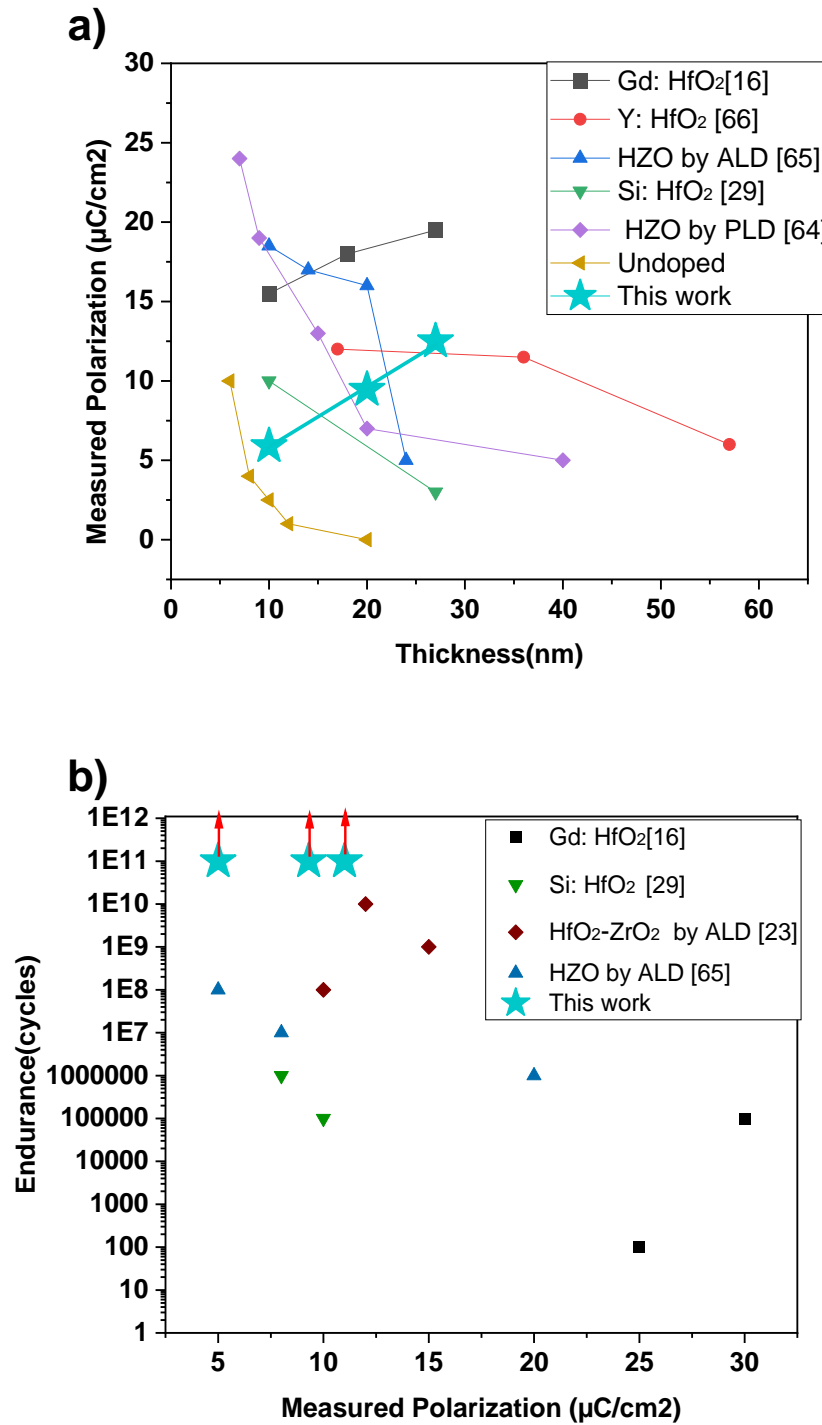


Figure 4.20: (a) A comparative study of remnant polarization depending upon thickness for different dopants (Undoped HfO₂[2], HZO by ALD [3], HZO by PLD [4], Si: HfO₂ [5], Y: HfO₂ [6], Gd: HfO₂ [7]), (b) Endurance vs P_r diagram for various reported result compared with this study.

4.2.3 Depth Profile Analysis

To determine the intermixing, if any, between the HfO₂ and ZrO₂ layer, XPS depth profile measurements were taken in every 2 second interval during ion etching of the sample from the surface to the bottom of TiN electrode. An argon ion source having energy 4000 eV was used for etching. Figure 4.21 (a) and (b) show the profile of the HfO₂ and ZrO₂ signal for 2 structures grown at different temperatures. The profiles were determined by analyzing the high-resolution spectra of Zr 3d and Hf 4f peaks as shown in figure 4.22.

From region 1, only signal of ZrO₂ is obvious; signal from other elements is entirely absent. As etching continues, i.e., in region 2, ZrO₂ signal begins to decay while signal of HfO₂ starts to appear as expected from the interface of two layers. In region 3, signal of ZrO₂ is totally absent and HfO₂ appears as the dominant signal. Finally, further etching reveals the bottom electrode TiN. On the other hand, in case of 750 °C deposition temperature, ZrO₂ shows a significant amount of atomic percentage even in region 3. That means ZrO₂ diffused into the HfO₂ layer. To further verify the inter-diffusion or intermixing, a high-resolution scan of Hf 4f and Zr 3d were performed at the three separate regions as shown in figure 4.22. It is obvious from region 1 that only Zr 3d peak is present and in region 2, both Hf and Zr peaks appear. Finally, there is still a detectable peak of Zr 3d in region 3 along with the dominant peak Hf 4f. The presence of Zr 3d in region 3, sample grown at high temperature, confirms the inter-diffusion of ZrO₂ into HfO₂ layer. However, the composition of HfO₂ and ZrO₂ in the intermixing layer is difficult to determine because of the penetration depth of X-rays (~10nm). Transmission

electron microscopy (TEM) and Secondary Ion Mass Spectroscopy (SIMS) can be better alternative to validate the compositional percentage of the intermixing layer.

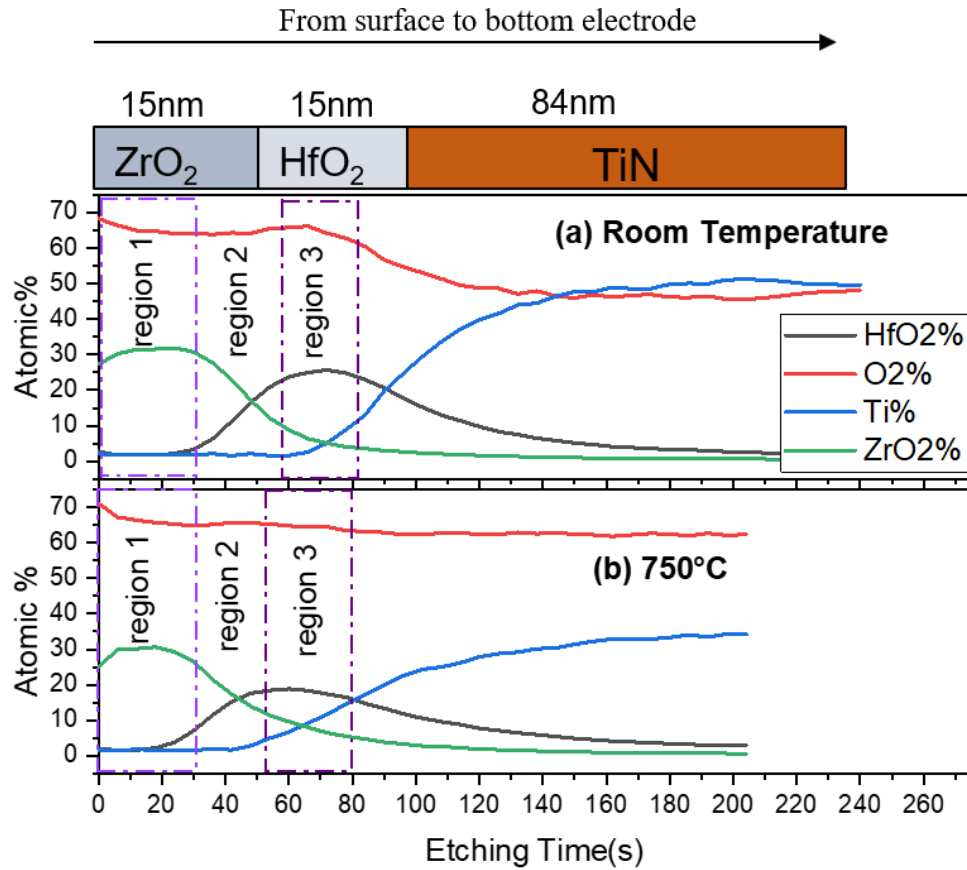


Figure 4.21: Etching profile of 15 nm HfO₂/15 nm ZrO₂. Atomic percentage of different compound vs etching time from surface to bottom electrode.

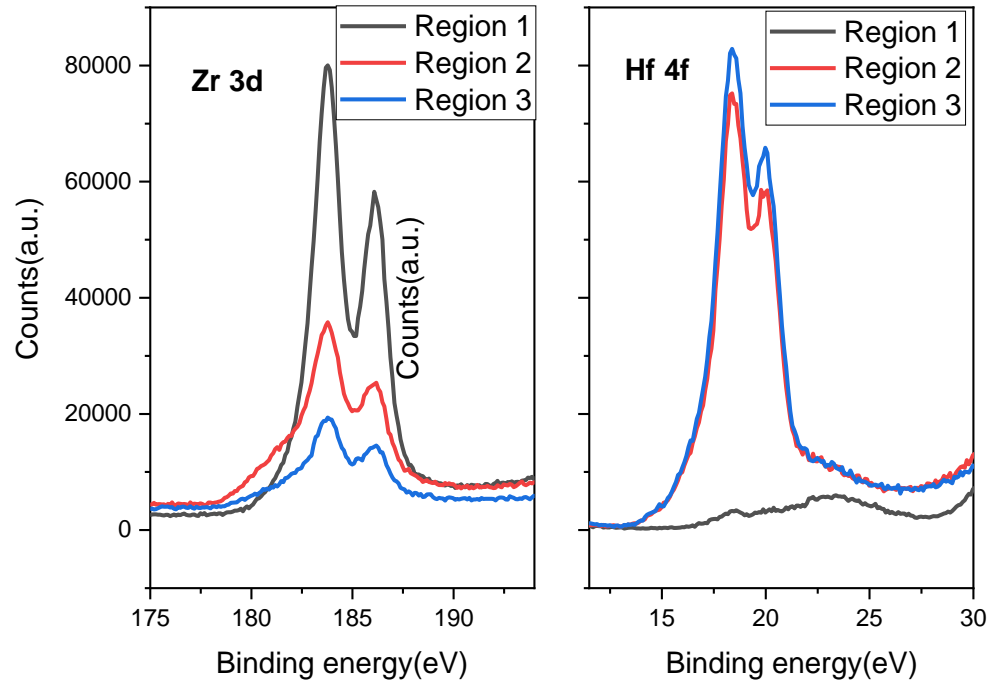


Figure 4.22: Comparison of Zr 3d and Hf 4f peaks at different etching regions at high temperature (750°C).

5. CONCLUSION AND FUTURE WORK

5.1 Conclusion

In conclusion, this study systematically examined the structural features and ferroelectric performances of HfO₂-ZrO₂ nanolaminates of different stack sequence and superlattice structure as a function of deposition conditions. Firstly, it was identified that ZrO₂ as top layer provides better ferroelectric performance than when used as the bottom layer. The ZrO₂ has a higher degree of crystallinity that result in a dominant monoclinic phase in the top HfO₂ layer. Secondly, thicker samples showed higher amount of o (002) phase fraction than thinner samples. Besides, higher pressure and higher temperature promoted the ferroelectric phase in the film resulted from the higher o (002) phase fraction. On the other hand, lower oxygen pressure and lower temperature could not stabilize ferroelectric phase in the structures. Based on the electrical properties of various nanolaminates and superlattice, superlattice structure showed reduced polarization compared to a bilayer structure and the 15 nm HfO₂/15 nm ZrO₂ structure deposited at 750°C and 1.24x10⁻² torr oxygen pressure achieved the most promising properties. This structure could endure more than 10¹² cycles with 11 μC/cm² remnant polarization which is much higher than the best result reported for HfO₂/ZrO₂ nanolaminates and solid solution films. Therefore, the study shows that nanolaminates structure of HfO₂-ZrO₂ can be highly promising for solid state electronics and potential energy related applications.

5.2 Future Work

Leakage current was a critical factor for thinner sample while measuring polarization. Post deposition annealing for longer duration might improve leakage

response by increasing grain size. Moreover, interfacial layer needed further studying by TEM and SIMS to verify the compositional percentage. Moreover, superlattice structure of $\text{HfO}_2\text{-ZrO}_2$ nanolaminates can be investigated further altering layer thicknesses to improve ferroelectric response. Finally, YSZ/ITO substrate can be used instead of TiN/SiO₂/Si, because YSZ/ITO acts as a good template for epitaxial growth of single crystalline films.

REFERENCES

- [1] R. C. Ribera, *Growth and thermal oxidation of Ru and ZrO₂ thin films as oxidation protective layers* Roger Coloma Ribera. .
- [2] P. Polakowski and J. Müller, “Ferroelectricity in undoped hafnium oxide,” *Appl. Phys. Lett.*, vol. 106, no. 23, p. 232905, 2015.
- [3] M. Hyuk Park, H. Joon Kim, Y. Jin Kim, T. Moon, and C. Seong Hwang, “The effects of crystallographic orientation and strain of thin Hf_{0.5}Zr_{0.5}O₂ film on its ferroelectricity,” *Appl. Phys. Lett.*, vol. 104, no. 7, p. 72901, 2014, doi: 10.1063/1.4866008.
- [4] J. Lyu, I. Fina, R. Solanas, J. Fontcuberta, and F. Sánchez, “Growth window of ferroelectric epitaxial Hf_{0.5}Zr_{0.5}O₂ thin films,” *ACS Appl. Electron. Mater.*, vol. 1, no. 2, pp. 220–228, 2019.
- [5] U. Schroeder, C. S. Hwang, and H. Funakubo, *Ferroelectricity in Doped Hafnium Oxide: Materials, Properties and Devices*. Elsevier Science, 2019.
- [6] J. Müller *et al.*, “Ferroelectricity in yttrium-doped hafnium oxide,” *J. Appl. Phys.*, vol. 110, no. 11, p. 114113, 2011.
- [7] M. Hoffmann *et al.*, “Stabilizing the ferroelectric phase in doped hafnium oxide,” *J. Appl. Phys.*, vol. 118, no. 7, p. 72006, 2015.
- [8] M. S. Pandian, P. Ramasamy, and B. Kumar, “A comparative study of ferroelectric triglycine sulfate (TGS) crystals grown by conventional slow evaporation and unidirectional method,” *Mater. Res. Bull.*, vol. 47, no. 6, pp. 1587–1597, 2012.

- [9] R. S. Pease and G. E. Bacon, “Ferroelectric structure of potassium dihydrogen phosphate,” *Nature*, vol. 173, no. 4401, pp. 443–444, 1954.
- [10] J. Valasek, “Piezo-electric and allied phenomena in Rochelle salt,” *Phys. Rev.*, vol. 17, no. 4, p. 475, 1921.
- [11] J. Lu, W. Luo, J. Feng, and H. Xiang, “Unusual ferroelectricity in two-dimensional perovskite oxide thin films,” *Nano Lett.*, vol. 18, no. 1, pp. 595–601, 2018.
- [12] A. M. Rappe and A. M. Kolpak, “Ferroelectric ultrathin perovskite films.” Google Patents, 2013.
- [13] R. E. Cohen, “Origin of ferroelectricity in perovskite oxides,” *Nature*, vol. 358, no. 6382, pp. 136–138, 1992.
- [14] K. Kim and S. Lee, “Integration of lead zirconium titanate thin films for high density ferroelectric random access memory,” *J. Appl. Phys.*, vol. 100, no. 5, p. 51604, 2006.
- [15] L. W. Martin and A. M. Rappe, “Thin-film ferroelectric materials and their applications,” *Nat. Rev. Mater.*, vol. 2, no. 2, pp. 1–14, 2016.
- [16] C.-P. De Araujo, J. D. Cuchiaro, L. D. McMillan, M. C. Scott, and J. F. Scott, “Fatigue-free ferroelectric capacitors with platinum electrodes,” *Nature*, vol. 374, no. 6523, pp. 627–629, 1995.
- [17] B. H. Park, B. S. Kang, S. D. Bu, T. W. Noh, J. Lee, and W. Jo, “Lanthanum-substituted bismuth titanate for use in non-volatile memories,” *Nature*, vol. 401, no. 6754, pp. 682–684, 1999.

- [18] A. Chernikova *et al.*, “5Zr0.5O2 ferroelectric films on Si, ACS Appl. Mater. Interfaces (Providence), vol. 8, no. 11, 2016.
- [19] J. Müller *et al.*, “Ferroelectricity in HfO₂ enables nonvolatile data storage in 28 nm HKMG,” in *2012 Symposium on VLSI Technology (VLSIT)*, 2012, pp. 25–26.
- [20] X. Sang, E. D. Grimley, T. Schenk, U. Schroeder, and J. M. LeBeau, “On the structural origins of ferroelectricity in HfO₂ thin films,” *Appl. Phys. Lett.*, vol. 106, no. 16, p. 162905, 2015.
- [21] T. Shimizu *et al.*, “The demonstration of significant ferroelectricity in epitaxial Y-doped HfO₂ film,” *Sci. Rep.*, vol. 6, p. 32931, 2016.
- [22] Z. Fan, J. Chen, and J. Wang, “Ferroelectric HfO₂-based materials for next-generation ferroelectric memories,” *J. Adv. Dielectr.*, vol. 6, no. 02, p. 1630003, 2016.
- [23] K. D. Kim *et al.*, “Ferroelectricity in undoped-HfO₂ thin films induced by deposition temperature control during atomic layer deposition,” *J. Mater. Chem. C*, vol. 4, no. 28, pp. 6864–6872, 2016.
- [24] S. Starschich, T. Schenk, U. Schroeder, and U. Boettger, “Ferroelectric and piezoelectric properties of Hf_{1-x}Zr_xO₂ and pure ZrO₂ films,” *Appl. Phys. Lett.*, vol. 110, no. 18, p. 182905, 2017.
- [25] U. Schroeder *et al.*, “Impact of different dopants on the switching properties of ferroelectric hafniumoxide,” *Jpn. J. Appl. Phys.*, vol. 53, no. 8S1, p. 08LE02, 2014.

- [26] M. Hoffmann *et al.*, “Ferroelectric phase transitions in nanoscale HfO₂ films enable giant pyroelectric energy conversion and highly efficient supercapacitors,” *Nano Energy*, vol. 18, pp. 154–164, 2015.
- [27] R. Materlik, C. Künneth, and A. Kersch, “The origin of ferroelectricity in Hf_{1-x}Zr_xO₂: A computational investigation and a surface energy model,” *J. Appl. Phys.*, vol. 117, no. 13, p. 134109, 2015, doi: 10.1063/1.4916707.
- [28] M. H. Park *et al.*, “A comprehensive study on the structural evolution of HfO₂ thin films doped with various dopants,” *J. Mater. Chem. C*, vol. 5, no. 19, pp. 4677–4690, 2017, doi: 10.1039/C7TC01200D.
- [29] M. Shandalov and P. McIntyre, “Size-dependent polymorphism in HfO₂ nanotubes and nanoscale thin films,” *J. Appl. Phys.*, vol. 106, p. 84322, 2009.
- [30] E. Yurchuk *et al.*, “Impact of layer thickness on the ferroelectric behaviour of silicon doped hafnium oxide thin films,” *Thin Solid Films*, vol. 533, pp. 88–92, 2013, doi: 10.1016/j.tsf.2012.11.125.
- [31] H. J. Kim *et al.*, “Grain size engineering for ferroelectric Hf_{0.5}Zr_{0.5}O₂ films by an insertion of Al₂O₃ interlayer,” *Appl. Phys. Lett.*, vol. 105, no. 19, p. 192903, 2014.
- [32] C.-K. Lee, E. Cho, H.-S. Lee, C. S. Hwang, and S. Han, “First-principles study on doping and phase stability of HfO_2 ,” *Phys. Rev. B*, vol. 78, no. 1, p. 12102, Jul. 2008, doi: 10.1103/PhysRevB.78.012102.

- [33] Q. Zeng *et al.*, “Evolutionary search for new high-k dielectric materials: methodology and applications to hafnia-based oxides,” *Acta Crystallogr. Sect. C, Struct. Chem.*, vol. 70, no. Pt 2, pp. 76–84, Feb. 2014, doi: 10.1107/S2053229613027861.
- [34] A. Salamat, A. L. Hector, B. M. Gray, S. A. J. Kimber, P. Bouvier, and P. F. McMillan, “Synthesis of Tetragonal and Orthorhombic Polymorphs of Hf₃N₄ by High-Pressure Annealing of a Prestructured Nanocrystalline Precursor,” *J. Am. Chem. Soc.*, vol. 135, no. 25, pp. 9503–9511, Jun. 2013, doi: 10.1021/ja403368b.
- [35] T. D. Huan, V. Sharma, G. A. Rossetti, and R. Ramprasad, “Pathways towards ferroelectricity in hafnia,” *Phys. Rev. B*, vol. 90, no. 6, p. 64111, Aug. 2014, doi: 10.1103/PhysRevB.90.064111.
- [36] M. Hyuk Park, H. Joon Kim, Y. Jin Kim, W. Lee, T. Moon, and C. Seong Hwang, “Evolution of phases and ferroelectric properties of thin Hf_{0.5}Zr_{0.5}O₂ films according to the thickness and annealing temperature,” *Appl. Phys. Lett.*, vol. 102, no. 24, p. 242905, 2013.
- [37] D. Das, V. Gaddam, and S. Jeon, “Demonstration of High Ferroelectricity in Zr Rich Hf_xZr_{1-x}O₂ Films,” *IEEE Electron Device Lett.*, vol. 41, no. 1, pp. 34–37, 2019.
- [38] S. Y. Wang, F. Guo, X. Wang, W. F. Liu, and J. Gao, “Tuning the resistive switching memory in a metal–ferroelectric–semiconductor capacitor by field effect structure,” *Appl. Surf. Sci.*, vol. 356, pp. 898–904, 2015.

- [39] P. D. Lomenzo *et al.*, “Ferroelectric phenomena in Si-doped HfO₂ thin films with TiN and Ir electrodes,” *J. Vac. Sci. Technol. B, Nanotechnol. Microelectron. Mater. Process. Meas. Phenom.*, vol. 32, no. 3, p. 03D123, 2014.
- [40] M. Hyuk Park, H. Joon Kim, Y. Jin Kim, W. Lee, H. Kyeom Kim, and C. Seong Hwang, “Effect of forming gas annealing on the ferroelectric properties of Hf_{0.5}Zr_{0.5}O₂ thin films with and without Pt electrodes,” *Appl. Phys. Lett.*, vol. 102, no. 11, p. 112914, 2013.
- [41] M. H. Park *et al.*, “Study on the degradation mechanism of the ferroelectric properties of thin Hf_{0.5}Zr_{0.5}O₂ films on TiN and Ir electrodes,” *Appl. Phys. Lett.*, vol. 105, no. 7, p. 72902, 2014.
- [42] M. H. Park *et al.*, “A comprehensive study on the mechanism of ferroelectric phase formation in hafnia-zirconia nanolaminates and superlattices,” *Appl. Phys. Rev.*, vol. 6, no. 4, 2019, doi: 10.1063/1.5118737.
- [43] Y. W. Lu, J. Shieh, and F. Y. Tsai, “Induction of ferroelectricity in nanoscale ZrO₂/HfO₂ bilayer thin films on Pt/Ti/SiO₂/Si substrates,” *Acta Mater.*, vol. 115, pp. 68–75, 2016.
- [44] S. E. Reyes-Lillo, K. F. Garrity, and K. M. Rabe, “Antiferroelectricity in thin-film ZrO_2 from first principles,” *Phys. Rev. B*, vol. 90, no. 14, p. 140103, Oct. 2014, doi: 10.1103/PhysRevB.90.140103.
- [45] S. L. Weeks, A. Pal, V. K. Narasimhan, K. A. Littau, and T. Chiang, “Engineering of Ferroelectric HfO₂-ZrO₂ Nanolaminates,” *ACS Appl. Mater. Interfaces*, 2017, doi: 10.1021/acsami.7b00776.

- [46] M. Mattinen *et al.*, “Atomic layer deposition of iridium thin films using sequential oxygen and hydrogen pulses,” *J. Phys. Chem. C*, vol. 120, no. 28, pp. 15235–15243, 2016.
- [47] K. V Egorov, Y. Y. Lebedinskii, A. A. Soloviev, A. A. Chouprik, A. Y. Azarov, and A. M. Markeev, “Initial and steady-state Ru growth by atomic layer deposition studied by in situ Angle Resolved X-ray Photoelectron Spectroscopy,” *Appl. Surf. Sci.*, vol. 419, pp. 107–113, 2017.
- [48] T. Shimizu, T. Yokouchi, T. Shiraishi, T. Oikawa, P. S. S. R. Krishnan, and H. Funakubo, “Study on the effect of heat treatment conditions on metalorganic-chemical-vapor-deposited ferroelectric Hf_{0.5}Zr_{0.5}O₂ thin film on Ir electrode,” *Jpn. J. Appl. Phys.*, vol. 53, no. 9S, p. 09PA04, 2014.
- [49] S. Starschich, S. Menzel, and U. Böttger, “Evidence for oxygen vacancies movement during wake-up in ferroelectric hafnium oxide,” *Appl. Phys. Lett.*, vol. 108, no. 3, p. 32903, 2016.
- [50] T. Nakamura, Y. Nakao, A. Kamisawa, and H. Takasu, “Preparation of Pb (Zr, Ti) O₃ thin films on electrodes including IrO₂,” *Appl. Phys. Lett.*, vol. 65, no. 12, pp. 1522–1524, 1994.
- [51] D. Zhou *et al.*, “Wake-up effects in Si-doped hafnium oxide ferroelectric thin films,” *Appl. Phys. Lett.*, vol. 103, no. 19, p. 192904, 2013.
- [52] A. G. Chernikova *et al.*, “Improved ferroelectric switching endurance of La-doped Hf_{0.5}Zr_{0.5}O₂ thin films,” *ACS Appl. Mater. Interfaces*, vol. 10, no. 3, pp. 2701–2708, 2018.

- [53] S. J. Kim, J. Mohan, S. R. Summerfelt, and J. Kim, “Ferroelectric Hf 0.5 Zr 0.5 O₂ thin films: A review of recent advances,” *JOM*, vol. 71, no. 1, pp. 246–255, 2019.
- [54] C. N. Afonso, J. Gonzalo, R. Serna, and J. Solís, “Pulsed Laser Deposition for Functional Optical Films,” in *Laser Ablation and its Applications*, C. Phipps, Ed. Boston, MA: Springer US, 2007, pp. 315–338.
- [55] Y. R. Herrero and A. Ullah, “14 - Metal oxide powder technologies in catalysis,” in *Metal Oxide Powder Technologies*, Y. Al-Douri, Ed. Elsevier, 2020, pp. 279–297.
- [56] N. M. Bulgakova, R. Stoian, A. Rosenfeld, I. V Hertel, and E. E. B. Campbell, “Fast Electronic Transport and Coulomb Explosion in Materials Irradiated with Ultrashort Laser Pulses,” in *Laser Ablation and its Applications*, C. Phipps, Ed. Boston, MA: Springer US, 2007, pp. 17–36.
- [57] D. Dijkkamp *et al.*, “Preparation of Y-Ba-Cu oxide superconductor thin films using pulsed laser evaporation from high T_c bulk material,” *Appl. Phys. Lett.*, vol. 51, no. 8, pp. 619–621, 1987, doi: 10.1063/1.98366.
- [58] K. Moorjani *et al.*, “Superconductivity in bulk and thin films of La_{1.85}Sr,” *Phys. Rev. B. Condens. Matter*, vol. 36, no. 7, pp. 4036–4038, Sep. 1987, doi: 10.1103/physrevb.36.4036.

- [59] J. Pou, F. Lusquiños, R. Comesaña, and M. Boutinguiza, “Chapter 14 - Production of Biomaterial Coatings by Laser-Assisted Processes☆,” in *Advances in Laser Materials Processing (Second Edition)*, Second Edi., J. Lawrence, Ed. Woodhead Publishing, 2018, pp. 381–412.
- [60] “X-Ray Diffraction Methods,” in *Materials Characterization*, John Wiley & Sons, Ltd, 2008, pp. 45–77.
- [61] M. Yasaka, “X-ray thin-film measurement techniques V . X-ray reflectivity measurement,” 2010.
- [62] “Scanning Probe Microscopy,” in *Materials Characterization*, John Wiley & Sons, Ltd, 2013, pp. 163–189.
- [63] R. Secondo *et al.*, “Reliable modeling of ultrathin alternative plasmonic materials using spectroscopic ellipsometry Invited,” *Opt. Mater. Express*, vol. 9, no. 2, pp. 760–770, Feb. 2019, doi: 10.1364/OME.9.000760.
- [64] J. Bouaziz, P. Rojo Romeo, N. Baboux, and B. Vilquin, “Characterization of ferroelectric hafnium/zirconium oxide solid solutions deposited by reactive magnetron sputtering,” *J. Vac. Sci. Technol. B, Nanotechnol. Microelectron. Mater. Process. Meas. Phenom.*, vol. 37, no. 2, p. 21203, 2019.
- [65] M. Burke *et al.*, “Low sheet resistance titanium nitride films by low-temperature plasma-enhanced atomic layer deposition using design of experiments methodology,” *J. Vac. Sci. Technol. A*, vol. 32, no. 3, p. 31506, 2014, doi: 10.1116/1.4868215.

- [66] Y. H. Lee *et al.*, "Preparation and characterization of ferroelectric Hf_{0.5}Zr_{0.5}O₂ thin films grown by reactive sputtering," *Nanotechnology*, vol. 28, no. 30, p. 305703, 2017.